A non-classical couple stress based Mindlin plate finite element framework for tuning band gaps of periodic composite micro plates

Zixu Xia, Gongye Zhang, Yu Cong, Shuitao Gu

A non-classical couple stress based Mindlin plate finite element framework for tuning band gaps of periodic composite micro plates

Z. X. Xia [a], **G. Y. Zhang** [b], **Y. Cong** [c] *, **S. T. Gu** [a] *,

[a] *School of Civil Engineering, Chongqing University, Chongqing 400044, China*
[b] *Jiangsu Key Laboratory of Engineering Mechanics, School of Civil Engineering, Southeast University, Nanjing, Jiangsu 210096, China*
[c] *Université Paris-Saclay, Univ Evry, LMEE, 91020, Evry, France*

Abstract

Composite micro plates with periodic microstructure at very small length scale have been a focus of intensive research. When length scale of the microstructure descends below millimetre level, size effects may emerge. To account for microstructure effect on the elastic wave band gap of microscopic composite plates, we propose a numerical framework based on the modified couple stress theory of elasto-dynamics associated with a non-classical 3-node triangular (T3) Mindlin plate finite element. Since couple stress elasto-dynamics incorporates dependence on the material scale length, the proposed approach is sensitive to size effects with microscopic problems while remaining compatible with macroscopic problems. In terms of the finite element implementation, we implemented a T3 plate finite element with 9 nodal degrees of freedom under the Mindlin kinematics assumptions. The approach presents enhanced flexibility to discretize complex microstructures owing to the triangular element topology, and offers sensitivity to account for size effects of microscopic problems. Therefore, it represents a good option for the design of band gap periodic composite micro plates. Validation of the framework is performed through comparison with both analytical and numerical models.

Keywords: Band gap; Composite micro plate; Couple stress theory; Mindlin plate

1 Introduction

Band gap composites ([1][2][3][4][5]) are a family of architectured materials that offer tunable properties to influence wave propagation according to the wave frequency. An important property of these materials is the band gap ([6][7][8][9][10]) characteristics, which specifically designates the capacity to hinder propagation of waves in particular frequency ranges.

The formation mechanism of band gap is mainly determined by two phenomena ([11]) : the first involves elastic wave scattering ([12]) which takes place on the material or structure interface; the other, based on resonance effect ([13]), results from local vibration of the resonator which absorbs

* Corresponding authors:
yu.cong@univ-evry.fr (Y. Cong),
gust@cqu.edu.cn (S. T. Gu).

Preprint
Mar. 2022

energy of the elastic wave, leading to vibration attenuation. Both mechanisms require that the material microstructure be designed at scales under the order of the wavelengths of the phenomena they influence. This leads frequently to micro-scale localized microstructures, for which size dependent effects ([14]) may emerge. Due to the presence of size effects, band gaps of microstructures cannot be accurately determined using classical theories of elasto-dynamics since they lack adapted constitutive description that incorporates dependence on the material scale length.

To address the issue of size effects, a variety of high-order theories of elasticity have been proposed recently to describe size-dependent band gap behaviours. For example, Zhang et al. ([15]) developed a modified couple stress theory to determine elastic wave band gaps for 3D phononic crystals. Madeo et al. ([16]) developed relaxed linear micromorphic continuum theory for elastic wave control of finite-size metastructures. Chen ([17]) proposed a new set of non-classical wave equations to investigate layered phononic crystals. Based on the high-order continuum theories, several size-dependent micro beam ([18, 19]), plate ([20, 21, 22, 23]) and shell ([24, 25]) models have been recently developed to study microscopic thin structures. Among these achievements, only a few models provide numerical solution with finite element formulation. In fact, finite element implementation of high-order continuum theories is not a trivial task. It requires interpolation of nodal parameters that satisfy at least $C1$ continuity since second-order derivatives of the displacement are involved. However, strict $C1$ continuous interpolation is difficult to construct and leads to either important number of nodal parameters ([26, 27]), or complex element structures ([28, 29]). Until recently, only a few examples of $C1$ continuous elements have been successfully implemented based on high-order continuum theories ([30, 31, 32]). Alternatively, instead of seeking strict $C1$ continuity, one may only require a relaxed but tolerable compatibility for the displacement field by using non-conforming element formulations. Non-conforming elements may be discontinuous for the displacement derivatives on the inter-element boundary, but preserve $C1$ continuity at the nodes. Furthermore, they are relatively simple to implement ([33]).

In this paper, we implemented a T3 plate finite element with 9 nodal degrees of freedom, whose interpolation functions were proposed by Bazeley ([34]). We then extended the Bazeley element to Mindlin kinematics in the context of couple stress continuum theory. The aim is to solve band gap problems involving microstructures of small length scales for which size effects are no longer negligible. To capture the size effect, we introduce symmetric curvature tensor into the kinematic relations, which leads to high-order strain, then the associated work conjugate yields couple stress. The high-order stress and strains are related by a constitutive model which incorporates dependence on the material length scale. The finite element framework takes advantage of triangular element topology, which offers improved flexibility to discretize complex geometries. We implemented vibration modal analysis based on Bloch-Floquet periodic boundary conditions, which allows band gap calculations that we validated through comparison with both theoretical and comparative numerical models.

To describe the proposed numerical framework, we organize the article as follows: we start by presenting in Section 2, the theoretical formulation of the band gap unit cell problem based on modified couple stress theory. Then in Section 3, we provide details on the implementation of the non-classical Mindlin micro plate finite element. In Section 4, periodic boundary conditions based on Bloch-Floquet theory is applied, which leads to the formulation of the band gap problem to be solved. We note that the term "wave finite element method" is frequently used in the literature to designate numerical implementation given in Section 3 and 4. In Section 5, 3 numerical examples are provided to validate and discuss the implemented numerical framework. In the end, conclusion remarks are drawn in Section 6.

2 Band gap unit cell problem with modified couple stress theory

Size effects may emerge in band gap composite micro plates when the microstructure length scale approaches millimetre level. To capture the effect of size dependence, a modified couple stress model is implemented through a unit cell problem that represents the material's microstructure.

2.1 Modified couple stress theory

Elasto-statics of the modified couple stress theory was first proposed by Yang et al. [35] based on the principle of minimum potential energy. According to this theory, strain energy U for an isotropic deformable body Ω, within linear elasticity integrates contributions due to both classical Cauchy strain and symmetric curvature tensors:

$$U = \frac{1}{2}\int_{\Omega} (\boldsymbol{\sigma} : \boldsymbol{\varepsilon} + \boldsymbol{m} : \boldsymbol{\chi})\, \mathrm{d}V, \tag{1}$$

where $\mathrm{d}V$ is the unit volume. $\boldsymbol{\sigma}$ and $\boldsymbol{m}$ are, respectively, the components of the Cauchy stress and deviatoric part of the couple stress tensors. Then accordingly, $\boldsymbol{\varepsilon}$ and $\boldsymbol{\chi}$ are, respectively the components of Cauchy strain and symmetric curvature tensors given by

$$\boldsymbol{\varepsilon} = \frac{1}{2}\left(\nabla \boldsymbol{u} + (\nabla \boldsymbol{u})^T\right), \tag{2}$$

$$\boldsymbol{\chi} = \frac{1}{2}\left(\nabla \boldsymbol{\theta} + (\nabla \boldsymbol{\theta})^T\right), \tag{3}$$

in which $\boldsymbol{u}$ are the displacement vector and $\boldsymbol{\theta}$ refer to the rotation vector, defined as

$$\boldsymbol{\theta} = \frac{1}{2}\nabla \times \boldsymbol{u}, \tag{4}$$

with ∇ being the Hamiltonian operator, "$\times$" denoting the cross product symbol, which will be kept in the following. Constitutive relations in the modified couple stress theory, involving expressions of Cauchy stress and couple stress tensors, are written as

$$\begin{cases} \boldsymbol{\sigma} = \lambda \mathrm{tr}\,(\boldsymbol{\varepsilon})\,\mathbf{I} + 2\mu\boldsymbol{\varepsilon} \\ \boldsymbol{m} = 2\mu l^2 \boldsymbol{\chi} \end{cases}, \tag{5}$$

where $\mathbf{I}$ is second order unit tensor. λ and μ are the Lamé constants according to classical elasticity. l is a material length scale parameter, it measures the couple stress effect ([36][37]) and is commonly determined experimentally.

2.2 Couple stress band gap unit cell problem

Consider the region Π, occupied by a periodic bi-phase composite micro plate comprising inclusions (Phase I) embedded periodically in a host matrix (Phase II) represented in Fig.(1). The composite plate Π is significantly larger in dimension compared to its unit cell Ω whose mid-surface representation is also shown in Fig.(1). The depicted unit cell Ω is considered to be composed of material points $p \subset \mathbb{R}^3$. Location of point p can be indicated by the position vector $\mathbf{r}$, defined within the basis formed by three perpendicular basis vectors $\mathbf{a}_1$, $\mathbf{a}_2$ and $\mathbf{a}_3$, with $\mathbf{a}_1$, $\mathbf{a}_2$ forming a plane that coincides with the unit

cell's lower surface, and $\mathbf{a}_3$ in the plate through-thickness direction, so that $\mathbf{r} = A_1\mathbf{a}_1 + A_2\mathbf{a}_2 + A_3\mathbf{a}_3$ for $A_1, A_2, A_3 \in [0, 1]$. Since periodic composite micro plates are concerned, only in-plane heterogeneities exist, thus $\mathbf{a}_1$ and $\mathbf{a}_2$ also correspond to the material periodicity. This means in-plane disposition of material heterogeneities across the medium varies periodically according to $\mathbf{a}_1$ and $\mathbf{a}_2$, such that

$$\lambda(\mathbf{r} + n_i\mathbf{a}_i) = \lambda(\mathbf{r}), \qquad \mu(\mathbf{r} + n_i\mathbf{a}_i) = \mu(\mathbf{r}), \qquad \rho(\mathbf{r} + n_i\mathbf{a}_i) = \rho(\mathbf{r}), \quad \text{with } i = 1, 2 \tag{6}$$

with ρ the material density, λ and μ the elastic constants, and $n_i \in \mathbb{Z}$.

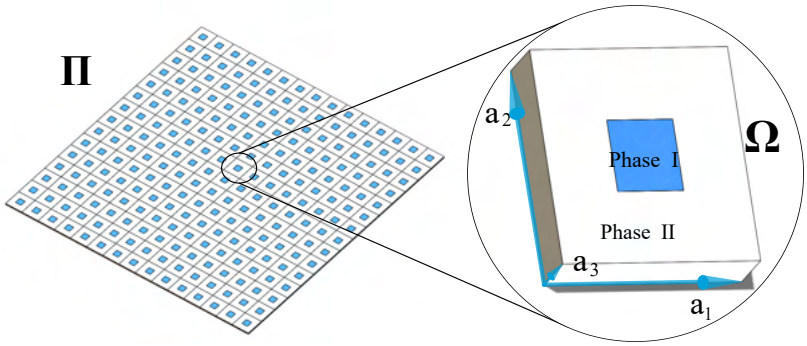

Figure 1: Example of a periodic composite micro plate and its unit cell

Propagation of elastic waves in solids is governed by the equation of elasto-dynamics. Here, to address the microstructure effects, the governing equation of classical elasto-dynamics is written in the context of modified couple stress theory ([38]), which gives

$$\nabla \cdot \boldsymbol{\sigma} - \frac{1}{2}\nabla \times (\nabla \cdot \mathbf{m}) - \frac{1}{2}\nabla \times \mathbf{c} + \mathbf{f} = \rho\ddot{\mathbf{u}} \, . \tag{7}$$

This gives the equation of motion for all points in Ω at any $t \in (0, T)$, with "$\cdot$" denoting the dot product symbol, which will be kept in the following; $\boldsymbol{\sigma}$ and $\mathbf{m}$ related by the constitutive equation (Eq.5); $\mathbf{c}$ and $\mathbf{f}$, referring respectively to the components of body couple (moment per unit volume) and body force (force per unit volume) acting on Ω; then $\mathbf{u}$ the components of displacement vector. The displacement field in Ω, as a result of elastic wave propagation, is a harmonic function based on time and the position vector, described by

$$\mathbf{u}(\mathbf{r}, t) = \mathbf{u}(\mathbf{r})e^{i\omega t} \, , \tag{8}$$

in which ω refers to angular frequency. Applying the Bloch-Floquet theorem ([39]), we transform the harmonic description (Eq.8) of the displacement field of Ω as

$$\mathbf{u}(\mathbf{r}, \mathbf{k}) = \mathbf{u}_k(\mathbf{r})e^{i(\mathbf{k}\cdot\mathbf{r})} \, , \tag{9}$$

where $\mathbf{k} = (k_x, k_y)$ refers to Bloch vector, $\mathbf{u}_k(\mathbf{r})$ is a periodic function of the same material periodicity as the region Π, namely $\mathbf{a}_i$ $(i = 1, 2)$. Finally, the displacement field satisfies

$$\begin{aligned} \mathbf{u}_k\left(\mathbf{r} + \mathbf{a}_i\right) &= \mathbf{u}_k \\ \mathbf{u}(\mathbf{r} + \mathbf{a}_i, \mathbf{k}) &= \mathbf{u}_k(\mathbf{r} + \mathbf{a}_i)e^{i(\mathbf{k}\cdot\mathbf{r})}e^{i(\mathbf{k}\cdot\mathbf{a}_i)} \\ \mathbf{u}(\mathbf{r} + \mathbf{a}_i, \mathbf{k}) &= \mathbf{u}_k\left(\mathbf{r}\right)e^{i(\mathbf{k}\cdot\mathbf{a}_i)} \, . \end{aligned} \tag{10}$$

The above relationships (Eq.10) allow developing the Bloch boundary conditions based on the unit cell

Ω and its governing equation Eq.7, formulated according to the couple stress theory.

Bloch Boundary value problem: strong form

Considering Eq.(7,10), we summarize the unit cell Bloch boundary value problem with the strong form as follows:

$$\begin{cases} \nabla \cdot \boldsymbol{\sigma} - \frac{1}{2}\nabla \times (\nabla \cdot \mathbf{m}) - \frac{1}{2}\nabla \times \mathbf{c} + \mathbf{f} = \rho \ddot{\mathbf{u}} \\ \mathbf{u}(\mathbf{r} + \mathbf{a}_i, \mathbf{k}) = \mathbf{u}_k(\mathbf{r})\, e^{i(\mathbf{k}\cdot\mathbf{a}_i)} \end{cases} . \tag{11}$$

Bloch Boundary value problem: weak form

To facilitate finite element implementation for the resolution of the unit cell Bloch boundary value problem, we transform the strong formulation of the governing equation (Eq.11.1) into its weak form equivalent. Using the standard procedure based on the principle of virtual work, we obtain

$$\begin{cases} \int_T \int_\Omega (\delta\boldsymbol{\varepsilon} : \boldsymbol{\sigma} + \delta\boldsymbol{\chi} : \boldsymbol{m}) \mathrm{d}V \mathrm{d}t = \int_T \int_\Omega \rho \ddot{\mathbf{u}} : \delta\ddot{\mathbf{u}} \mathrm{d}V \mathrm{d}t \\ \mathbf{u}(\mathbf{r} + \mathbf{a}_i, \mathbf{k}) = \mathbf{u}_k(\mathbf{r})\, e^{i(\mathbf{k}\cdot\mathbf{a}_i)} \end{cases} . \tag{12}$$

by considering integration on time domain T with the absence of body forces or external loads. The left side of the equation gives the internal virtual work, and the right side of the equation refers to the mass kinetic energy from the virtual work.

3 Implementation of a Mindlin micro plate T3 finite element

In this section, a T3 plate finite element with 9 degrees of freedom is implemented and extended to the Mindlin kinematic assumptions. We start by presenting basic equations of the Mindlin micro plate in Section 3.1, where Mindlin kinematic relations are adapted in the context of couple stress theory. In Section 3.2, the shape functions were first published by Bazeley ([34]), which we adopt to interpolate nodal kinematic parameters involving displacements and their derivatives. Then in Section 3.3, we provide transformation between the global and the natural coordinates which allows better understanding the finite element implementation.

3.1 Basic equations

Let us consider a plate structure of uniform thickness t shown in Fig.(2). The plate is subject to uniform force load q, and in-plane couple (pure moment) load m_x and m_y, respectively around x and y axis. We use $u(x, y, z)$, $v(x, y, z)$ and $w(x, y, z)$ to denote displacement components along x, y and z axis. Then, we use $u(x, y)$, $v(x, y)$ and $w(x, y)$ to refer to displacement components of the middle plane, and accordingly, $\phi_x(x, y)$, $\phi_y(x, y)$ the rotation components of the middle plane.

The proposed plate element is developed under the assumptions of vibroacoustic analysis, in respect of the basic kinematic rules of Mindlin plate theory ([40]), that we recall as follows: (1) The plate thickness remains constant during deformation. (2) Normal stress through the thickness remains negligeable, which is known as the *plane-stress* assumption. (3) Linear variation of displacement across the plate thickness is allowed. As a result, the cross section remains flat during deformation, but not necessarily perpendicular to the mid-surface.

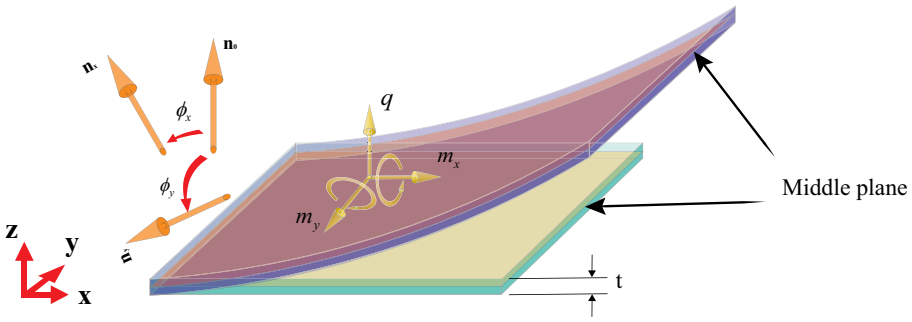

Figure 2: Plate structure configuration

From assumptions (1)-(3), displacement components of the proposed plate formulation can be derived:

$$\begin{aligned} u(x,y,z) &= u_0(x,y) - z\phi_x(x,y) \\ v(x,y,z) &= v_0(x,y) - z\phi_y(x,y) \\ w(x,y,z) &= w(x,y). \end{aligned} \tag{13}$$

Then from assumption (4), we can define the section angle as a combination of bending angle and shear angle which is shown in Fig.(2), so

$$\begin{aligned} \phi_x &= \frac{\partial w}{\partial x} + \beta_x \\ \phi_y &= \frac{\partial w}{\partial y} + \beta_y \ , \end{aligned} \tag{14}$$

where β_x, β_y refer to shear angles with respect ot $x-$axis and $y-$axis, respectively.

Cauchy strain ε expression

Based on the Mindlin kinematic relations Eq.(13,14) and the definition of Cauchy strain (Eq.(2)), we obtain expressions of the Cauchy strain vector:

$$\boldsymbol{\varepsilon} = \left\{ \begin{array}{c} \varepsilon_x \\ \varepsilon_y \\ \gamma_{xy} \\ \hdashline \gamma_{xz} \\ \gamma_{yz} \end{array} \right\} = \left\{ \begin{array}{c} \frac{\partial u_0}{\partial x} - z\frac{\partial \phi_x}{\partial x} \\ \frac{\partial v_0}{\partial y} - z\frac{\partial \phi_y}{\partial y} \\ \hdashline \left[\frac{\partial u_0}{\partial y} + \frac{\partial v_0}{\partial x}\right] - z\left[\frac{\partial \phi_x}{\partial y} + \frac{\partial \phi_y}{\partial x}\right] \\ \hdashline \frac{\partial w_0}{\partial x} - \phi_x \\ \frac{\partial w_0}{\partial y} - \phi_y \end{array} \right\} = \mathbf{S}_\varepsilon \left\{ \begin{array}{c} \hat{\boldsymbol{\varepsilon}}_b \\ \hdashline \hat{\boldsymbol{\varepsilon}}_s \end{array} \right\}, \tag{15}$$

for which in-plane and out-of-plane strain components are collected separately, and noted distinctly by $\hat{\boldsymbol{\varepsilon}}_b$ and $\hat{\boldsymbol{\varepsilon}}_s$. The obtained strain vector $\boldsymbol{\varepsilon}$ can be further decoupled into the product of transformation matrix $\mathbf{S}_\varepsilon$ and generalized strain $\hat{\boldsymbol{\varepsilon}}$:

$$\boldsymbol{\varepsilon} = \mathbf{S}_\varepsilon \hat{\boldsymbol{\varepsilon}} \ , \tag{16}$$

where the transformation matrix $\mathbf{S}_\varepsilon$ writes

$$\mathbf{S}_\varepsilon = \begin{bmatrix} 1 & -z & 0 & 0 & 0 & 0 & 0 & 0 \\ 0 & 0 & 1 & -z & 0 & 0 & 0 & 0 \\ 0 & 0 & 0 & 0 & 1 & -z & 0 & 0 \\ 0 & 0 & 0 & 0 & 0 & 0 & 1 & 0 \\ 0 & 0 & 0 & 0 & 0 & 0 & 0 & 1 \end{bmatrix} , \tag{17}$$

and the generalized strain $\hat{\boldsymbol{\varepsilon}}$ consists of bending term $\hat{\boldsymbol{\varepsilon}}_b$ and shear deformation term $\hat{\boldsymbol{\varepsilon}}_s$

$$\hat{\boldsymbol{\varepsilon}} = \left\{ \begin{array}{c} \hat{\boldsymbol{\varepsilon}}_b \\ \hdashline \hat{\boldsymbol{\varepsilon}}_s \end{array} \right\} = \left\{ \begin{array}{c} \frac{\partial u_0}{\partial x} \\ \frac{\partial \phi_x}{\partial x} \\ \frac{\partial v_0}{\partial y} \\ \frac{\partial \phi_y}{\partial y} \\ \frac{\partial u_0}{\partial y} + \frac{\partial v_0}{\partial x} \\ \frac{\partial \phi_x}{\partial y} + \frac{\partial \phi_y}{\partial x} \\ \hdashline \frac{\partial w}{\partial x} - \phi_x \\ \frac{\partial w}{\partial y} - \phi_y \end{array} \right\}. \tag{18}$$

Symmetric curvature tensor $\boldsymbol{\chi}$ expression

Symmetric curvature tensor Eq.(3) derives from the rotation vector $\boldsymbol{\theta}$, which is defined based on the plate kinematic parameters including displacement (Eq.(13)) and section angle variation (Eq.(14)). Hence, the rotation vector with the account for Mindlin plate kinematics can be written as

$$\boldsymbol{\theta} = \left[\begin{array}{c} \theta_x \\ \theta_y \\ \theta_z \end{array} \right] = \frac{1}{2} \left[\begin{array}{c} \frac{\partial w}{\partial y} + \phi_y \\ -\frac{\partial w}{\partial x} - \phi_x \\ \frac{\partial v_0}{\partial x} - \frac{\partial u_0}{\partial y} - z\frac{\partial \phi_y}{\partial x} + z\frac{\partial \phi_x}{\partial y} \end{array} \right]. \tag{19}$$

We now derive $\boldsymbol{\theta}$ components and by using Eq.(3), we obtain the expression of symmetric curvature tensor $\boldsymbol{\chi}$

$$\boldsymbol{\chi} = \left[\begin{array}{c} \chi_x \\ \chi_y \\ \chi_z \\ \chi_{xy} \\ \chi_{xz} \\ \chi_{yz} \end{array} \right] = \left[\begin{array}{c} \frac{\partial \theta_x}{\partial x} \\ \frac{\partial \theta_y}{\partial y} \\ \frac{\partial \theta_z}{\partial z} \\ \frac{1}{2}\left(\frac{\partial \theta_x}{\partial y} + \frac{\partial \theta_y}{\partial x}\right) \\ \frac{1}{2}\left(\frac{\partial \theta_x}{\partial z} + \frac{\partial \theta_z}{\partial x}\right) \\ \frac{1}{2}\left(\frac{\partial \theta_y}{\partial z} + \frac{\partial \theta_z}{\partial y}\right) \end{array} \right] = \frac{1}{4} \left[\begin{array}{c} 2\left(\frac{\partial^2 w}{\partial y \partial x} + \frac{\partial \phi_y}{\partial x}\right) \\ -2\left(\frac{\partial^2 w}{\partial x \partial y} + \frac{\partial \phi_x}{\partial y}\right) \\ -2\left(\frac{\partial \phi_y}{\partial x} - \frac{\partial \phi_x}{\partial y}\right) \\ \left(\frac{\partial^2 w}{\partial y^2} + \frac{\partial \phi_y}{\partial y}\right) - \left(\frac{\partial^2 w}{\partial x^2} + \frac{\partial \phi_x}{\partial x}\right) \\ \left(\frac{\partial^2 v_0}{\partial x^2} - \frac{\partial^2 u_0}{\partial x \partial y}\right) - z\left(\frac{\partial^2 \phi_y}{\partial x \partial y} - \frac{\partial^2 \phi_x}{\partial y^2}\right) \\ \left(\frac{\partial^2 v_0}{\partial x \partial y} - \frac{\partial^2 u_0}{\partial y^2}\right) - z\left(\frac{\partial^2 \phi_y}{\partial x^2} - \frac{\partial^2 \phi_x}{\partial y \partial x}\right) \end{array} \right]. \tag{20}$$

We proceed the same way as for Cauchy strain, and formulate $\boldsymbol{\chi}$ as the product of transformation matrix $\mathbf{S}_\chi$, and generalized curvature $\hat{\boldsymbol{\chi}}$, hence

$$\boldsymbol{\chi} = \mathbf{S}_\chi \hat{\boldsymbol{\chi}}\,, \tag{21}$$

with the transformation matrix

$$\mathbf{S}_\chi = \begin{bmatrix} \frac{1}{2} & 0 & 0 & 0 & 0 & 0 & 0 & 0 \\ 0 & -\frac{1}{2} & 0 & 0 & 0 & 0 & 0 & 0 \\ 0 & 0 & -\frac{1}{2} & 0 & 0 & 0 & 0 & 0 \\ 0 & 0 & 0 & \frac{1}{4} & 0 & 0 & 0 & 0 \\ 0 & 0 & 0 & 0 & \frac{1}{4} & -\frac{z}{4} & 0 & 0 \\ 0 & 0 & 0 & 0 & 0 & 0 & \frac{1}{4} & -\frac{z}{4} \end{bmatrix}, \tag{22}$$

and the generalized curvature

$$\hat{\boldsymbol{\chi}} = \begin{pmatrix} \frac{\partial^2 w}{\partial y \partial x} + \frac{\partial \phi_y}{\partial x} \\ \frac{\partial^2 w}{\partial x \partial y} + \frac{\partial \phi_x}{\partial y} \\ \frac{\partial \phi_y}{\partial x} - \frac{\partial \phi_x}{\partial y} \\ \left(\frac{\partial^2 w}{\partial y^2} + \frac{\partial \phi_y}{\partial y}\right) - \left(\frac{\partial^2 w}{\partial x^2} + \frac{\partial \phi_x}{\partial x}\right) \\ \frac{\partial^2 v_0}{\partial x^2} - \frac{\partial^2 u_0}{\partial x \partial y} \\ \frac{\partial^2 \phi_y}{\partial x \partial y} - \frac{\partial^2 \phi_x}{\partial y^2} \\ \frac{\partial^2 v_0}{\partial x \partial y} - \frac{\partial^2 u_0}{\partial y^2} \\ \frac{\partial^2 \phi_y}{\partial x^2} - \frac{\partial^2 \phi_x}{\partial y \partial x} \end{pmatrix} . \tag{23}$$

Constitutive relations

With previously obtained expressions of Cauchy strain $\boldsymbol{\varepsilon}$ (Eq.(16)), and symmetric curvature $\boldsymbol{\chi}$ (Eq.(21)), we can readily calculate stress tensors, which in the couple stress theory, consist of classical Cauchy stress and couple stress tensors as provided by Eq.(5). Therefore, we can write Cauchy stress tensor as

$$\boldsymbol{\sigma} = \mathbf{D}_\varepsilon \boldsymbol{\varepsilon} \, , \tag{24}$$

with the classical elasticity matrix $\mathbf{D}_\varepsilon$ given by Eq.(5).1, hence

$$\mathbf{D}_\varepsilon = \begin{bmatrix} \frac{E}{1-\nu^2} & \frac{vE}{1-\nu^2} & 0 & 0 & 0 \\ \frac{vE}{1-\nu^2} & \frac{E}{1-\nu^2} & 0 & 0 & 0 \\ 0 & 0 & \frac{E}{2(1+\nu)} & 0 & 0 \\ 0 & 0 & 0 & k_{11}G & 0 \\ 0 & 0 & 0 & 0 & k_{22}G \end{bmatrix} , \tag{25}$$

and Cauchy strain $\boldsymbol{\varepsilon}$ calculated in Eq.(16). Similarly, we can express the couple stress tensor $\mathbf{m}$ based on Eq.(5).2. Therefore

$$\mathbf{m} = \mathbf{D}_\chi \boldsymbol{\chi} \, , \tag{26}$$

where the elasticity matrix based on couple stress theory writes

$$\mathbf{D}_\chi = \begin{bmatrix} 2Gl^2 & 0 & 0 & 0 & 0 & 0 \\ 0 & 2Gl^2 & 0 & 0 & 0 & 0 \\ 0 & 0 & 2Gl^2 & 0 & 0 & 0 \\ 0 & 0 & 0 & 2Gl^2 & 0 & 0 \\ 0 & 0 & 0 & 0 & 2Gl^2 & 0 \\ 0 & 0 & 0 & 0 & 0 & 2Gl^2 \end{bmatrix} . \tag{27}$$

Note that in the above expressions Eq.(25,27), G refers to shear modulus, E is Young's modulus, ν is Possion's ratio, and k_{11}, k_{22} are in-plane shear correction parameters, which in this article, take the following value $k_{11} = k_{22} = \frac{5}{6}$.

Generalized stress and couple stress

In the proposed Mindlin plate finite element, we prescribe pre-integration of constitutive relations through the plate thickness. This allows using integration scheme based on the plate mid-surface. Therefore, we integrate previously calculated Cauchy stress $\boldsymbol{\sigma}$ (Eq.(24)) and couple stress $\boldsymbol{m}$ (Eq.(26))

in the plate thickness direction which leads to generalized stress and couple stress

$$\begin{cases} \hat{\boldsymbol{\sigma}} = \int_{-\frac{t}{2}}^{\frac{t}{2}} \mathbf{S}_{\varepsilon}^{T} \boldsymbol{\sigma} \mathrm{d}z = \hat{\mathbf{D}}_{\varepsilon} \hat{\boldsymbol{\varepsilon}} \\ \hat{\mathbf{m}} = \int_{-\frac{t}{2}}^{\frac{t}{2}} \mathbf{S}_{\chi}^{T} \mathbf{m} \mathrm{d}z = \hat{\mathbf{D}}_{\chi} \hat{\boldsymbol{\chi}} \end{cases}, \tag{28}$$

in which

$$\begin{aligned} \hat{\mathbf{D}}_{\varepsilon} &= \int_{-\frac{t}{2}}^{\frac{t}{2}} \mathbf{S}_{\varepsilon}^{T} \mathbf{D}_{\varepsilon} \mathbf{S}_{\varepsilon} \mathrm{d}z \\ \hat{\mathbf{D}}_{\chi} &= \int_{-\frac{t}{2}}^{\frac{t}{2}} \mathbf{S}_{\chi}^{T} \mathbf{D}_{\chi} \mathbf{S}_{\chi} \mathrm{d}z \end{aligned}. \tag{29}$$

3.2 Implementation of the interpolation functions

The formulation of couple stress elasticity involves first and second derivatives of displacements due to the symmetric curvature tensor(Eq.(20)). We implement in this work a non-conforming interpolation scheme ([34]) permitting nodal continuity of displacements and their first order derivatives.

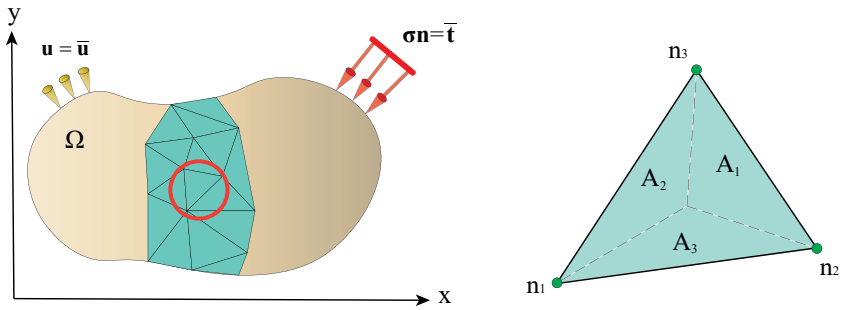

Figure 3: Illustration of 3 node triangular (T3) finite element for non-classical Mindlin micro plate with C^1 continuity. The element consists of 3 partitions, with A_i $(i = 1, 2, 3)$ referring to the area of each partition.

The following 9 order polynomials are used to obtain approximation of kinematic field variables via interpolation. This involves in particular the in-of-plane displacement u_0, v_0, the out-of-plane displacement w , and rotations around x and y axis, ϕ_x and ϕ_y respectively. In the following, approximation of the out-of-plane displacement w is given as an example. The other 4 parameters follow the same polynomial approximation.

$$\begin{aligned} w = \quad & a_1 L_1 + a_2 L_2 + a_3 L_3 \\ & + a_4 \left(L_1^2 L_2 + \frac{L_1 L_2 L_3}{2} \right) + a_5 \left(L_2^2 L_1 + \frac{L_1 L_2 L_3}{2} \right) \\ & + a_6 \left(L_2^2 L_3 + \frac{L_1 L_2 L_3}{2} \right) + a_7 \left(L_3^2 L_2 + \frac{L_1 L_2 L_3}{2} \right) \\ & + a_8 \left(L_3^2 L_1 + \frac{L_1 L_2 L_3}{2} \right) + a_9 \left(L_1^2 L_3 + \frac{L_1 L_2 L_3}{2} \right) \end{aligned} \tag{30}$$

where L_i $(i = 1, 2, 3)$ refers to area coordinates. As shown in Figure 3, the parameter L_i indicates area proportion of the ith partition with respect to the element area, which means, $L_1 = \frac{A_1}{A}$, $L_2 = \frac{A_2}{A}$, $L_3 = \frac{A_3}{A}$ and $L_1 + L_2 + L_3 = 1$, with A_i the area of the ith partition and A the element area. Except L_i which can be calculated knowing the element configuration, the remaining parameters a_i $(i = 1, \cdots 9)$

are undetermined coefficients. According to the relations of area coordinates, only two coordinates are independent. We therefore define triangular natural coordinates s and t. The relationship between the area coordinates and the natural coordinates is defined as $L_2 = s$, $L_3 = t$ and $L_1 = 1-s-t$. Solving the undetermined coefficients requires determination of the displacement field of vertical deflection, using the following formulation

$$\begin{aligned} w_i = \quad & a_1 L_{1i} + a_2 L_{2i} + a_3 L_{3i} \\ & + a_4 \left(L_{1i}^2 L_{2i} + \frac{L_{1i} L_{2i} L_{3i}}{2} \right) + a_5 \left(L_{2i}^2 L_{1i} + \frac{L_{1i} L_{2i} L_{3i}}{2} \right) \\ & + a_6 \left(L_{2i}^2 L_{3i} + \frac{L_{1i} L_{2i} L_{3i}}{2} \right) + a_7 \left(L_{3i}^2 L_{2i} + \frac{L_{1i} L_{2i} L_{3i}}{2} \right) \\ & + a_8 \left(L_{3i}^2 L_{1i} + \frac{L_{1i} L_{2i} L_{3i}}{2} \right) + a_9 \left(L_{1i}^2 L_{3i} + \frac{L_{1i} L_{2i} L_{3i}}{2} \right) \end{aligned} \tag{31}$$

$$\begin{aligned} \frac{dw_i}{ds} = \quad & a_2 + a_5 \left(2\, L_{1i}\, L_{2i} + \frac{L_{1i}\, L_{3i}}{2} \right) \\ & + a_6 \left(\frac{L_{1i}\, L_{3i}}{2} + 2\, L_{2i}\, L_{3i} \right) + a_4 \left(L_{1i}^2 + \frac{L_{3i}\, L_{1i}}{2} \right) \\ & + a_7 \left(L_{3i}^2 + \frac{L_{1i}\, L_{3i}}{2} \right) + \frac{L_{1i}\, L_{3i}\, a_8}{2} + \frac{L_{1i}\, L_{3i}\, a_9}{2} \end{aligned} \tag{32}$$

$$\begin{aligned} \frac{dw_i}{dt} = \quad & a_3 + a_7 \left(\frac{L_{1i}\, L_{2i}}{2} + 2\, L_{2i}\, L_{3i} \right) \\ & + a_8 \left(\frac{L_{1i}\, L_{2i}}{2} + 2\, L_{1i}\, L_{3i} \right) + a_6 \left(L_{2i}^2 + \frac{L_{1i}\, L_{2i}}{2} \right) \\ & + a_9 \left(L_{1i}^2 + \frac{L_{2i}\, L_{1i}}{2} \right) + \frac{L_{1i}\, L_{2i}\, a_4}{2} + \frac{L_{1i}\, L_{2i}\, a_5}{2} \\ & (i = 1, 2, 3) \ . \end{aligned} \tag{33}$$

Solving Eq.(31-33) determines 3 unknowns specific to out-of-plane deflection w_i. By considering 5 fields of kinematic parameters involving 3 displacements and 2 rotations, we solve in total 15 unknown coefficients on 1 node. The approximate displacement field can be written in the form of shape functions and node displacements as follows:

$$\begin{aligned} u_0 &= \sum_{i=1}^{3} N_i u_{0i} + N_{is} \frac{\partial u_{0i}}{\partial s} + N_{it} \frac{\partial u_{0i}}{\partial t} \\ v_0 &= \sum_{i=1}^{3} N_i v_{0i} + N_{is} \frac{\partial v_{0i}}{\partial s} + N_{it} \frac{\partial v_{0i}}{\partial t} \\ w &= \sum_{i=1}^{3} N_i w_i + N_{is} \frac{\partial w_i}{\partial s} + N_{it} \frac{\partial w_i}{\partial t} \quad , \\ \phi_x &= \sum_{i=1}^{3} N_i \phi_{xi} + N_{is} \frac{\partial \phi_{xi}}{\partial s} + N_{it} \frac{\partial \phi_{xi}}{\partial t} \\ \phi_y &= \sum_{i=1}^{3} N_i \phi_{yi} + N_{is} \frac{\partial \phi_{yi}}{\partial s} + N_{it} \frac{\partial \phi_{yi}}{\partial t} \end{aligned} \tag{34}$$

where

$$\begin{cases} N_1 = L_1 + L_1^2 L_2 + L_1^2 L_3 - L_1 L_2^2 - L_1 L_3^2 \\ N_{1s} = b_2\left(L_1^2 L_3 + L\right) - b_3\left(L_2 L_1^2 + L\right) \\ N_{1t} = c_2\left(L_1^2 L_3 + L\right) - c_3\left(L_2 L_1^2 + L\right) \\ N_2 = L_2 + L_2^2 L_3 + L_2^2 L_1 - L_2 L_3^2 - L_2 L_1^2 \\ N_{2s} = b_3\left(L_2^2 L_1 + L\right) - b_1\left(L_3 L_2^2 + L\right) \\ N_{2t} = c_3\left(L_2^2 L_1 + L\right) - c_1\left(L_3 L_2^2 + L\right) \\ N_3 = L_3 + L_3^2 L_1 + L_3^2 L_2 - L_3 L_1^2 - L_3 L_2^2 \\ N_{3s} = b_1\left(L_3^2 L_2 + L\right) - b_2\left(L_1 L_3^2 + L\right) \\ N_{3t} = c_1\left(L_3^2 L_2 + L\right) - c_2\left(L_1 L_3^2 + L\right) \end{cases}, \tag{35}$$

with

$$L = \frac{L_1 L_2 L_3}{2} \quad b_i = y_j - y_m \quad c_i = x_m - x_j.$$

Within the proposed interpolation scheme, every element is associated with 45 degrees of freedom, which involve not only displacement and rotation variables, but also their derivatives. Therefore, element nodal displacement vector is of 45×1 size and can be written as

$$\mathbf{u}^{(q)} = \left[\, u_{01}\ v_{01}\ w_1\ \phi_{x1}\ \phi_{y1}\ \tfrac{\partial u_{01}}{\partial x}\ \tfrac{\partial v_{01}}{\partial x}\ \tfrac{\partial w_1}{\partial x}\ \tfrac{\partial \phi_{x1}}{\partial x}\ \tfrac{\partial \phi_{y1}}{\partial x}\ \tfrac{\partial u_{01}}{\partial y}\ \tfrac{\partial v_{01}}{\partial y}\ \tfrac{\partial w_1}{\partial y}\ \tfrac{\partial \phi_{x1}}{\partial y}\ \tfrac{\partial \phi_{y1}}{\partial y}\ \ldots \right]^T_{1\times 45} . \tag{36}$$

Using approximation by Eq.(34) and shape functions Eq.(35), we obtain the interpolated element displacment vector $\mathbf{u}^{(e)}$ in matrix form

$$\mathbf{u}^{(e)} = \mathbf{N} \cdot \mathbf{u}^{(q)} , \tag{37}$$

where $\mathbf{u}^{(q)}$ is given by Eq.(36), $\mathbf{N}$ is shape function matrix that writes

$$\mathbf{N} = \begin{bmatrix} N_1 & 0 & 0 & 0 & 0 & N_{1s} & 0 & 0 & 0 & 0 & N_{1t} & 0 & 0 & 0 & 0 & \cdots \\ 0 & N_1 & 0 & 0 & 0 & 0 & N_{1s} & 0 & 0 & 0 & 0 & N_{1t} & 0 & 0 & 0 & \cdots \\ 0 & 0 & N_1 & 0 & 0 & 0 & 0 & N_{1s} & 0 & 0 & 0 & 0 & N_{1t} & 0 & 0 & \cdots \\ 0 & 0 & 0 & N_1 & 0 & 0 & 0 & 0 & N_{1s} & 0 & 0 & 0 & 0 & N_{1t} & 0 & \cdots \\ 0 & 0 & 0 & 0 & N_1 & 0 & 0 & 0 & 0 & N_{1s} & 0 & 0 & 0 & 0 & N_{1t} & \cdots \end{bmatrix} , \tag{38}$$

and the interpolated element displacement vector $\mathbf{u}^{(e)}$ writes

$$\mathbf{u}^{(e)} = \begin{bmatrix} u_0 \\ v_0 \\ w \\ \phi_x \\ \phi_y \end{bmatrix} . \tag{39}$$

Generalized strain and generalized curvature expressions

At this stage with the shape function matrix fully developed for the T3 Mindlin micro plate element, we are ready to relate generalized strain $\hat{\boldsymbol{\varepsilon}}$ and curvature tensors $\hat{\boldsymbol{\chi}}$ to the vector of nodal kinematic variables $\mathbf{u}^{(q)}$. First for $\hat{\boldsymbol{\varepsilon}}$, we have

$$\hat{\boldsymbol{\varepsilon}} = \mathbf{B}_{\varepsilon} \mathbf{u}^{(q)} \tag{40}$$

where $\mathbf{B}_\varepsilon$ is the Cauchy strain-displacement matrix of dimension 8×45, which can be calculated by

$$\mathbf{B}_\varepsilon = \begin{bmatrix} \frac{\partial}{\partial x} & 0 & 0 & 0 & 0 \\ 0 & 0 & 0 & \frac{\partial}{\partial x} & 0 \\ 0 & \frac{\partial}{\partial y} & 0 & 0 & 0 \\ 0 & 0 & 0 & 0 & \frac{\partial}{\partial y} \\ \frac{\partial}{\partial y} & \frac{\partial}{\partial x} & 0 & 0 & 0 \\ 0 & 0 & 0 & \frac{\partial}{\partial y} & \frac{\partial}{\partial x} \\ 0 & 0 & \frac{\partial}{\partial x} & -1 & 0 \\ 0 & 0 & \frac{\partial}{\partial y} & 0 & -1 \end{bmatrix} \cdot \mathbf{N} \,, \tag{41}$$

with $\mathbf{N}$ the shape function matrix given by Eq.(38).

Similarly, we express generalized curvature tensors $\hat{\boldsymbol{\chi}}$ as function of the element nodal displacement $\mathbf{u}^{(q)}$

$$\hat{\boldsymbol{\chi}} = \mathbf{B}_\chi \mathbf{u}^{(q)} \tag{42}$$

where $\mathbf{B}_\chi$ is the curvature strain-displacement matrix of size 8×45, which can be calculated by

$$\mathbf{B}_\chi = \begin{bmatrix} 0 & 0 & \frac{\partial^2}{\partial y \partial x} & 0 & \frac{\partial}{\partial x} \\ 0 & 0 & \frac{\partial^2}{\partial x \partial y} & \frac{\partial}{\partial y} & 0 \\ 0 & 0 & 0 & -\frac{\partial}{\partial y} & \frac{\partial}{\partial x} \\ 0 & 0 & \frac{\partial^2}{\partial y^2} - \frac{\partial^2}{\partial x^2} & -\frac{\partial}{\partial x} & \frac{\partial}{\partial y} \\ -\frac{\partial^2}{\partial x \partial y} & \frac{\partial^2}{\partial x^2} & 0 & 0 & 0 \\ 0 & 0 & 0 & -\frac{\partial^2}{\partial y^2} & \frac{\partial^2}{\partial x \partial y} \\ -\frac{\partial^2}{\partial y^2} & \frac{\partial^2}{\partial x \partial y} & 0 & 0 & 0 \\ 0 & 0 & 0 & -\frac{\partial^2}{\partial y \partial x} & \frac{\partial^2}{\partial x^2} \end{bmatrix} \cdot \mathbf{N} \,, \tag{43}$$

with $\mathbf{N}$ given by Eq.(38). The Cauchy strain-displacement matrix $\mathbf{B}_\varepsilon$ and curvature strain-displacement matrix $\mathbf{B}_\chi$ are composed of shape function derivatives calculated with respect to global coordinates. The implementation using isoparametric element requires expressing their transformation between the global and natural coordinates, that we present in the next section.

3.3 Coordinates transformation

In this section, we provide the transformation of shape function derivatives between the natural coordinates and the global coordinates. This allows implementation of the finite element formulation using isoparametric method. Here, first order derivatives of the shape function are given as follows:

$$\begin{bmatrix} \frac{\partial N_i}{\partial s} \\ \frac{\partial N_i}{\partial t} \end{bmatrix} = \begin{bmatrix} \frac{\partial x}{\partial s} & \frac{\partial y}{\partial s} \\ \frac{\partial x}{\partial t} & \frac{\partial y}{\partial t} \end{bmatrix} \begin{bmatrix} \frac{\partial N_i}{\partial x} \\ \frac{\partial N_i}{\partial y} \end{bmatrix} . \tag{44}$$

The global coordinates can be written using the following interpolation:

$$\begin{aligned} x &= L_1 x_1 + L_2 x_2 + L_3 x_3 \\ y &= L_1 y_1 + L_2 y_2 + L_3 y_3 \end{aligned} . \tag{45}$$

Since only two area coordinates are independent, we can define $L_2 = s, L_3 = t, L_1 = 1 - s - t$, then derivates of the global coordinates are obtained:

$$\begin{aligned} \frac{\partial x}{\partial s} &= x_2 - x_1 \\ \frac{\partial x}{\partial t} &= x_3 - x_1 \\ \frac{\partial y}{\partial s} &= y_2 - y_1 \\ \frac{\partial y}{\partial t} &= y_3 - y_1 \end{aligned} . \tag{46}$$

Similarly, the second order derivatives of the shape function can be written as:

$$\begin{bmatrix} \frac{\partial^2 N_i}{\partial s^2} \\ \frac{\partial^2 N_i}{\partial s \partial t} \\ \frac{\partial^2 N_i}{\partial t \partial s} \\ \frac{\partial^2 N_i}{\partial t^2} \end{bmatrix} = \begin{bmatrix} \left(\frac{\partial x}{\partial s}\right)^2 & \frac{\partial y}{\partial s}\frac{\partial x}{\partial s} & \frac{\partial x}{\partial s}\frac{\partial y}{\partial s} & \left(\frac{\partial y}{\partial s}\right)^2 \\ \frac{\partial x}{\partial t}\frac{\partial x}{\partial s} & \frac{\partial y}{\partial t}\frac{\partial x}{\partial s} & \frac{\partial x}{\partial t}\frac{\partial y}{\partial s} & \frac{\partial y}{\partial t}\frac{\partial y}{\partial s} \\ \frac{\partial x}{\partial s}\frac{\partial x}{\partial t} & \frac{\partial y}{\partial s}\frac{\partial x}{\partial t} & \frac{\partial x}{\partial s}\frac{\partial y}{\partial t} & \frac{\partial y}{\partial s}\frac{\partial y}{\partial t} \\ \left(\frac{\partial x}{\partial t}\right)^2 & \frac{\partial y}{\partial t}\frac{\partial x}{\partial t} & \frac{\partial x}{\partial t}\frac{\partial y}{\partial t} & \left(\frac{\partial y}{\partial t}\right)^2 \end{bmatrix} \begin{bmatrix} \frac{\partial^2 N_i}{\partial x^2} \\ \frac{\partial^2 N_i}{\partial x \partial y} \\ \frac{\partial^2 N_i}{\partial y \partial x} \\ \frac{\partial^2 N_i}{\partial y^2} \end{bmatrix} . \tag{47}$$

We therefore obtain the transformation between the global and natural coordinates which allows implementation of the Cauchy strain-displacement matrix $\mathbf{B}_\varepsilon$ and curvature strain-displacement matrix $\mathbf{B}_\chi$ given in Eq.(41,43).

4 Implementation of unit cell boundary value problem

Considering the unit cell problem under conditions of free vibration, and using the matrices development provided in Section 3.1 and 3.2, we obtain finally the band gap unit cell boundary value problem whose implementation involves, on the one hand, the governing equation for unit cell modal analysis, and on the other, the boundary conditions.

Governing equation implementation

Let us first consider the governing equation of the couple stress unit cell problem in weak formulation (Eq.(12)), which can be implemented by using matrices developed in Section 3.1 and 3.2, under the form

$$\int_T \int_A \left[\left(\delta \mathbf{u}^{(e)}\right)^T \mathbf{B}_\varepsilon^T \hat{\mathbf{D}}_\varepsilon \mathbf{B}_\varepsilon \mathbf{u}^{(e)} + \left(\delta \mathbf{u}^{(e)}\right)^T \mathbf{B}_\chi^T \hat{\mathbf{D}}_\chi \mathbf{B}_\chi \mathbf{u}^{(e)} \right] dA dt = \int_T \int_\Omega \rho \delta \ddot{\mathbf{u}}^{(e)^T} \ddot{\mathbf{u}}^{(e)} dV dt \, . \tag{48}$$

Here, integration is performed on both the time and space domains. For the left part of the equation which corresponds to the internal virtual work, space domain integration is carried out on the mid-surface A of the unit cell Ω. This is because the formulation is based on generalized stress and generalized couple stress, both of which already incorporate through-thickness integration, as shown in Eq.(28-29). Since elastic wave propagation is under consideration, we introduce harmonic equation (Eq.(8)) of the displacement field $\mathbf{u}$ to Eq.(48), and we obtain the governing equation of free vibration:

$$\left[\mathbf{K} - \omega^2 \mathbf{M}\right] \mathbf{u}_0 = 0 \, , \tag{49}$$

where $\mathbf{u}_0$ is the mode shape vector of the unit cell, $\mathbf{K}$ is the stiffness matrix, which derives from Eq.(48)

and writes

$$\mathbf{K} = \int_A \mathbf{B}_\varepsilon^T \hat{\mathbf{D}}_\varepsilon \mathbf{B}_\varepsilon dA + \int_A \mathbf{B}_\chi^T \hat{\mathbf{D}}_\chi \mathbf{B}_\chi dA \,, \tag{50}$$

and $\mathbf{M}$ is the mass matrix which also derives from Eq.(48) and writes

$$\mathbf{M} = \int_A \mathbf{N}^\mathbf{T} \boldsymbol{\rho} \mathbf{N} dA \,, \tag{51}$$

with $\boldsymbol{\rho}$ the density matrix given by

$$\boldsymbol{\rho} = \begin{bmatrix} \rho t & 0 & 0 \\ 0 & \frac{\rho t^3}{12} & 0 \\ 0 & 0 & \frac{\rho t^3}{12} \end{bmatrix} . \tag{52}$$

Boundary conditions implementation

We now deal with implementation of the boundary conditions on the unit cell. Again we consider the unit cell illustration Ω presented in Section 2.2. Since only in-plane heterogeneities are under investigation, we depict the heterogeneous micro plate unit cell with its mid-surface as shown in Figure 4. The unit cell's lengths along the x and y axis are respectively a_1 and a_2, which also correspond to the microstructure periodicity along the respective axis. Node displacements on the unit cell boundary can be distinguished by nodes belonging to the 4 edges (outside the corner nodes), and the 4 corner nodes of the unit cell. Therefore, we use $\mathbf{u}_L$, $\mathbf{u}_R$, $\mathbf{u}_T$ and $\mathbf{u}_B$ to denote respectively nodal displacements on the left (L), right (R), top (T) and bottom (B) edges of the unit cell outside the corners. Then to make reference distinctly to the 4 corner nodes, we use $\mathbf{u}_{TL}$, $\mathbf{u}_{TR}$, $\mathbf{u}_{BL}$ and $\mathbf{u}_{BR}$ to denote respectively displacements of the top-left (TL), top-right (TR), bottom-left (BL) and bottom-right (BR) corner nodes. Accordingly, nodal displacements on the inner area of the domain, away from the boundary, are denoted by $\mathbf{u}_I$.

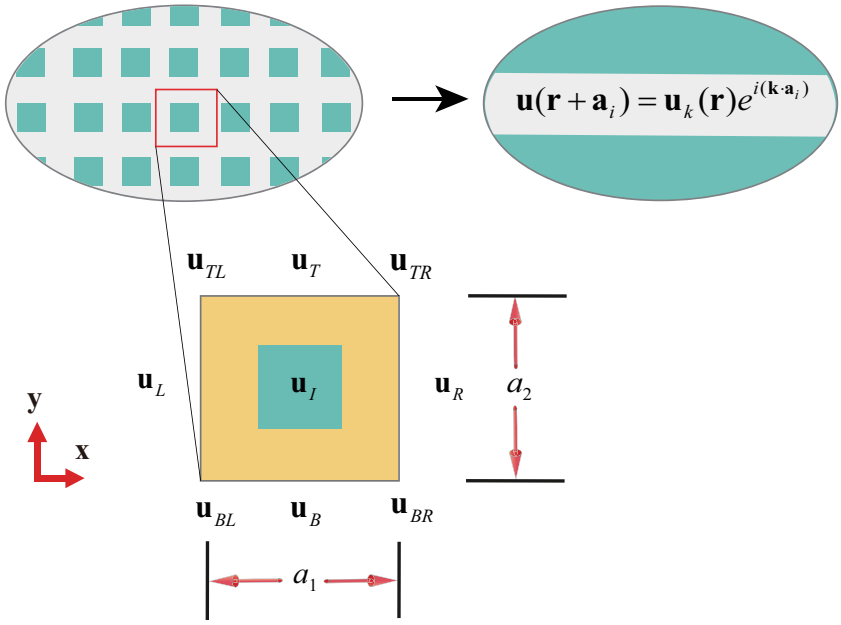

Figure 4: Mid-surface illustration of the bi-phase unit cell microstructure: we denote corner node displacements with $\mathbf{u}_{TL}$, $\mathbf{u}_{TR}$, $\mathbf{u}_{BL}$ and $\mathbf{u}_{BR}$, then edge node displacements with $\mathbf{u}_L$, $\mathbf{u}_R$, $\mathbf{u}_T$ and $\mathbf{u}_B$. Displacement of remaining nodes are collectively denoted by $\mathbf{u}_I$.

With the notation convention described above regarding the unit cell boundary nodes, we are ready

to implement the Bloch boundary conditions Eq.10. Let us consider $\lambda_1 = e^{i\boldsymbol{k}\cdot\boldsymbol{a_1}}$ and $\lambda_2 = e^{i\boldsymbol{k}\cdot\boldsymbol{a_2}}$, plus the condition of periodicity which allows relating $\mathbf{u}_R$ to $\mathbf{u}_L$, $\mathbf{u}_T$ to $\mathbf{u}_B$; then $\mathbf{u}_{BR}$, $\mathbf{u}_{TR}$ and $\mathbf{u}_{TL}$ to $\mathbf{u}_{BL}$, the displacement vector of the entire unit cell can be expressed as follows

$$\mathbf{u}_0 = \begin{bmatrix} \mathbf{u}_I \\ \mathbf{u}_L \\ \mathbf{u}_R \\ \mathbf{u}_B \\ \mathbf{u}_T \\ \mathbf{u}_{BL} \\ \mathbf{u}_{BR} \\ \mathbf{u}_{TR} \\ \mathbf{u}_{TL} \end{bmatrix} = \begin{bmatrix} \mathbf{I} & \mathbf{0} & \mathbf{0} & \mathbf{0} \\ \mathbf{0} & \mathbf{I} & \mathbf{0} & \mathbf{0} \\ \mathbf{0} & \lambda_1\mathbf{I} & \mathbf{0} & \mathbf{0} \\ \mathbf{0} & \mathbf{0} & \mathbf{I} & \mathbf{0} \\ \mathbf{0} & \mathbf{0} & \lambda_2\mathbf{I} & \mathbf{0} \\ \mathbf{0} & \mathbf{0} & \mathbf{0} & \mathbf{I} \\ \mathbf{0} & \mathbf{0} & \mathbf{0} & \lambda_1\mathbf{I} \\ \mathbf{0} & \mathbf{0} & \mathbf{0} & \lambda_1\lambda_2\mathbf{I} \\ \mathbf{0} & \mathbf{0} & \mathbf{0} & \lambda_2\mathbf{I} \end{bmatrix} \begin{bmatrix} \mathbf{u}_I \\ \mathbf{u}_L \\ \mathbf{u}_B \\ \mathbf{u}_{BL} \end{bmatrix} = \mathbf{P}\widetilde{\mathbf{u}} \,, \tag{53}$$

where $\widetilde{\mathbf{u}}$ collects the displacement on independent nodes I, L, B, and BL, depending on which displacement of other nodes can be deduced thanks to the structure periodicity. $\mathbf{I}$ is the identity matrix. Therefore, matrix $\mathbf{P}$ allows reducing the number of effective degrees of freedom of the unit cell problem, and is called transformation matrix.

By introducing Eq.(53) into the free vibration governing equation (Eq.(49)), we obtain the following expression

$$\left[\mathbf{K} - \omega^2\mathbf{M}\right]\mathbf{P}\widetilde{\mathbf{u}} = \mathbf{0} \,. \tag{54}$$

We consider $\mathbf{P}^\dagger$ that designates the conjugate transpose of $\mathbf{P}$ and transform Eq.(54) into

$$\mathbf{P}^\dagger\left[\mathbf{K} - \omega^2\mathbf{M}\right]\mathbf{P}\widetilde{\mathbf{u}} = \mathbf{0} \,. \tag{55}$$

Hence, we obtain the final form of the unit cell governing equation of free vibration with the account for Bloch boundary conditions, which writes

$$[\mathbf{K}_r - \omega^2\mathbf{M}_r]\widetilde{\mathbf{u}} = \mathbf{0} \,, \tag{56}$$

with

$$\begin{aligned} \mathbf{K}_r &= \mathbf{P}^\dagger\mathbf{K}\mathbf{P} \\ \mathbf{M}_r &= \mathbf{P}^\dagger\mathbf{M}\mathbf{P} \end{aligned} \,. \tag{57}$$

We can readily perform modal analysis based on Eq.(56-57) to solve the band gap unit cell problem as posed at the beginning of this work in the context of modified couple stress theory.

Numerical algorithm implementation

Resolution of the Bloch boundary value problem presented here is implemented using Matlab code that we developed for this work. The code involves finite element procedures for vibration modal analysis, implemented with Bloch boundary conditions on a periodic unit cell microstructure.

As shown in the flow chart, the algorithm requires looping on the points along the boundary of the irreducible first Brillouin zone (IBZ). On each of the points, a transform matrix $\mathbf{P}$ is calculated using Eq.(53), which leads to an independent vibration modal analysis. Bandgap result is obtained after repeating the calculation on all the nodes along the IBZ boundary.

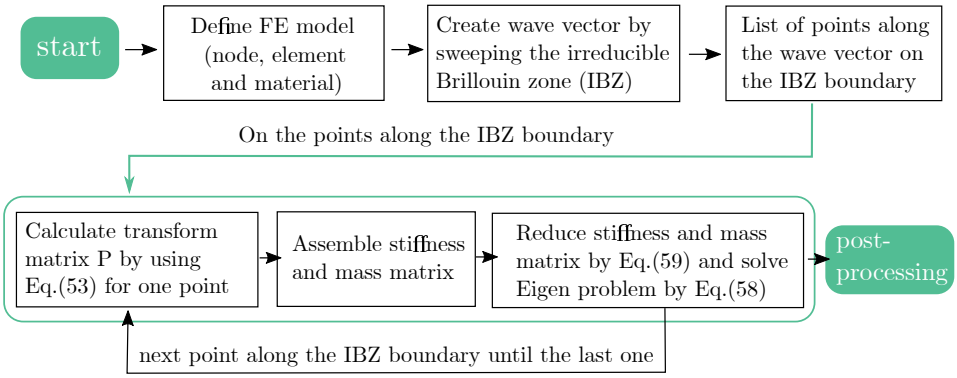

Figure 5: Algorithm flow chart: implementation of the Bloch boundary value problem on the T3 micro plate finite element unit cell.

5 Numerical results

In this section, the proposed band gap analysis framework will be investigated through 3 numerical cases. The first example, in Section 4.1, is aimed to validate the T3 couple stress Mindlin plate finite element through comparison with both analytical and numerical results based on the rectangular Adini-Clough-Melosh (ACM) plate element [41, 42]. For implementation details of the ACM element, readers are referred to [43]. Upon validation of the T3 element implementation, problems involving complex geometries will be studied, first in Section 4.2, to examine the influence of volume fraction on band gaps; then in Section 4.3, to investigate how width-thickness ratio affects the band gap in structures with chiral symmetry. We observe through numerical tests, that the implemented T3 couple stress Mindlin micro plate element fulfils the requirement for convergence performance, although its non-conforming formulation may lead to convergence difficulties, theoretically. We therefore conducted complementary tests with respect to the element's convergence properties. Results and analysis of these tests are provided as supplementary information. In all the test cases, numerical integration based on 3-point Gauss exact integration procedure is used. Details on the applied integration procedure are also given in the supplementary information.

5.1 Validation of the T3 couple stress Mindlin plate element implementation

In this example, we consider a classical bi-phase unit cell problem to validate the T3 couple stress Mindlin plate element implementation. The unit cell under consideration represents the microstructure of the periodically arranged bi-phase 2D metamaterial given in Fig.(1) from the theory Section 2.2. It is composed of a square matrix which incorporates a square inclusion at its centre. The unit cell is discretized first with the rectangular (ACM) element, then with the proposed T3 micro plate element. We perform band gap analysis for antiplane elastic waves using both mesh configurations and we consider the ACM model as the reference for comparison. To further validate the proposed numerical framework, comparison with analytical results based on plane wave expansion (PWE, we keep this abbreviation in the following) method ([44]) is provided.

The unit cell microstructure, depicted in Fig.(6a), is based on a square shape matrix of edge length $a = 1$ mm which contains at the centre a square inclusion of edge length $c = 0.4$ mm. This leads to an inclusion area ratio of 16% with respect to the whole cell area. Materials composing the unit cell can be distinguished between the inclusion material (phase I, iron) and the matrix material (phase II, epoxy),

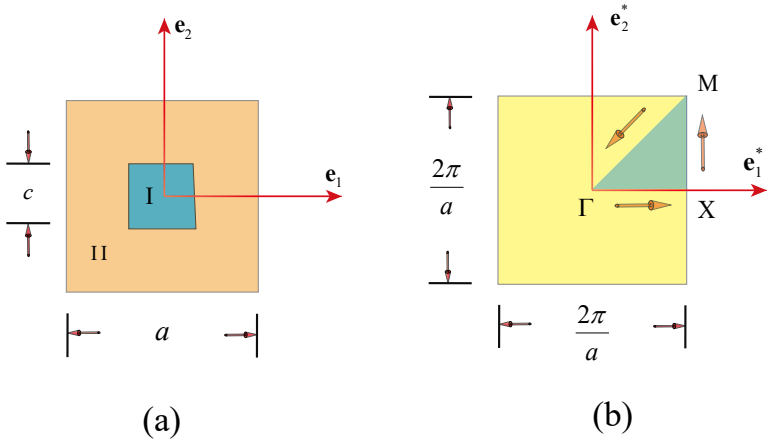

Figure 6: (a)Unit cell with rectangular inclusion (b)representation of the irreducible first Brillouin zone on the unit cell

Table 1: Material Group

Material	E (GPa)	v	l (μm)	ρ (g/cm^3)
Iron(Phase I)	177.33	0.27	6.76	7
Epoxy(Phase II)	3.3	0.33	16.93	1.18

whose properties are given in Table.1. The material size parameter l is calculated by $l = \frac{b_h}{\sqrt{3(1-v)}}$ ([45][46]), where b_h is the high-order bending parameter, v is Poisson's ratio, and the plate thickness $t = 120\mu m$ is considered.

Regarding the techniques for band gap analysis, as has been proven in ([47]), calculation of band diagrams only requires consideration of wave vectors on the boundary of the irreducible first Brillouin zone. Here, due to the presence of structure symmetry, our analysis can be reduced to the edges of the triangle $\Gamma - \mathrm{X} - \mathrm{M} - \Gamma$ as indicated in Fig.(6b). Numerically, this requires sweeping the boundary path $\Gamma - \mathrm{X} - \mathrm{M} - \Gamma$ by calculating on 58 equidistant, discrete points along the way. Then to perform finite element analysis on the unit cell model, we implement Floquet-periodic boundary conditions by considering the wave vector $\mathbf{k}_i = (k_x, k_y)$ $(i = 1, 2, \ldots, 58)$, which takes distinct forms on each section along the path $\Gamma - \mathrm{X} - \mathrm{M} - \Gamma$, in particular: from Γ to X, $k_x = \frac{2\pi}{a}k$, $k_y = 0$, $k \in [0, 1]$, from X to M, $k_x = \frac{2\pi}{a}$, $k_y = \frac{2\pi}{a}(k-1)$, $k \in [1, 2]$, from M to Γ, $k_x = \frac{2\pi}{a}(3-k)$, $k_y = \frac{2\pi}{a}(3-k)$, $k \in [2, 3]$. The unit cell is discretized with both the rectangular ACM element (as in Fig.(7)a,c) elements, and triangular (T3, as in Fig.(7)b,d) elements. Two sets of mesh refinement are applied, based on two edge seedings with 20 and 40 segments, respectively, shown in Fig.(7).

To further confirm the effectiveness of the implemented numerical framework, extra comparison with analytical results, here the PWE method, is provided. Application of analytical method explains the choice of the current unit cell microstructure, which only involves basic square geometries so as to accommodate the limitation of analytical analysis.

Band diagram results are reported in Fig.(8), where the diagrams (a) and (b) are obtained based on 20×20 and 40×40 mesh refinements, respectively. For each mesh refinement, results from the proposed T3 micro plate element is compared to the ACM model results. Let us first focus on diagrams (a). Here, excellent agreement is observed between the T3 and ACM results, especially in the lower frequency range where the T3 and ACM curves perfectly coincide. In the range of higher frequencies, T3 curves appear slightly above ACM results, though with insignificant differences. Also on diagram (a), we present the band curves obtained on the same problem setup, using analytical PWE method. Comparison between the PWE and finite element results reveals noticeable, yet tolerable differences,

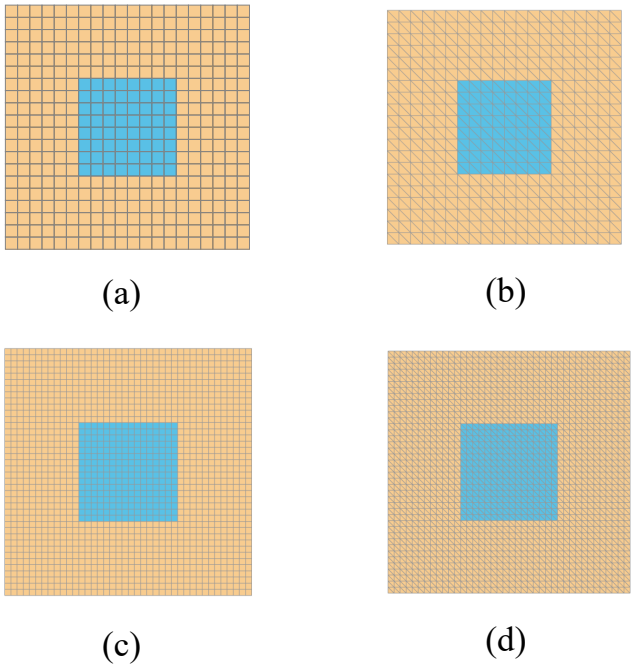

Figure 7: (a)Using 20 × 20 mesh with rectangular element to divide the cell (b)Using 20 × 20 mesh with triangular element to divide the cell (c)Using 40 × 40 mesh with rectangular element to divide the cell (d)Using 40 × 40 mesh with triangular element to divide the cell

mostly in the range of higher frequencies. Based on the above observations, we can conclude on the satisfactory accuracy that presents the proposed numerical framework based on T3 micro plate finite elements. We now move to diagram (b), which presents band diagrams obtained with further refined 40×40 meshes. Here, mesh refinement allowed even improved convergence of the T3 and ACM results, since difference between the compared mesh setups became barely noticeable. Meanwhile, we observed existance of a band gap situated between the fourth and fifth frequency curves, within the interval of [479.50, 525.76] kHz. This means that antiplane incident waves within this frequency range will be suppressed during its propagation in the investigated medium, whereas those outside the band gap frequency interval, will penetrate the medium and continue the propagation.

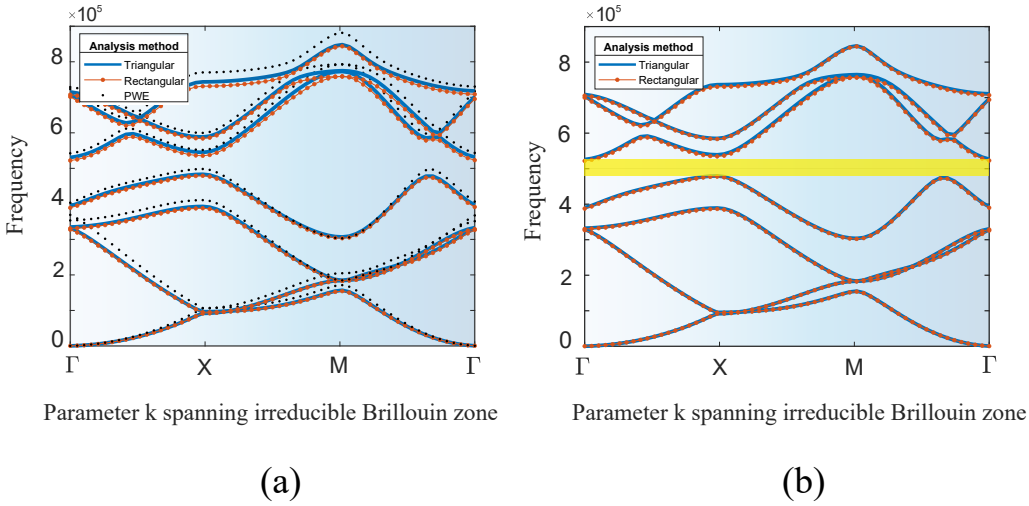

Figure 8: (a)Bang gap graph with grid density of 20 × 20 (b)Bang gap graph with grid density of 40 × 40

5.2 Effect of volume fraction

Upon validation of the T3 micro plate element for band gap analysis, we now extend its application to microstructures with complex geometry. Such microstructures cannot be efficiently studied by analytical methods, or by the ACM element due to the geometrical complexity. In this numerical case, we illustrate how the T3 micro plate element is applied on a microstructure involving an octagonal inclusion with varying shapes. Through this example, versatility of the proposed numerical method is demonstrated.

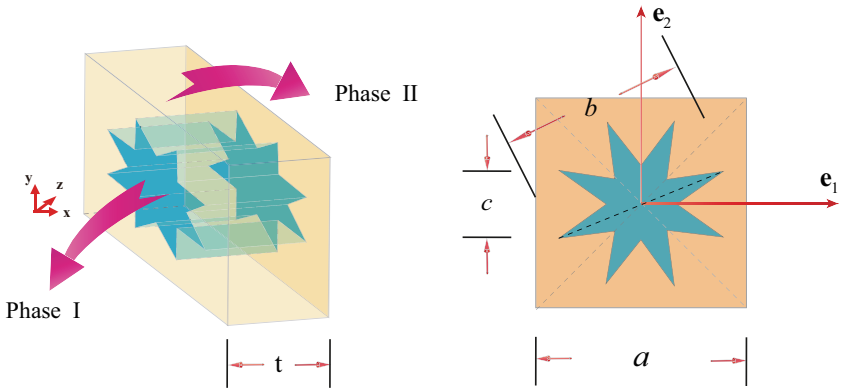

Figure 9: Illustration of the unit cell structure with octagonal star inclusion

The microstructure under consideration is modelled by a bi-phase unit cell with octagonal inclusion, as depicted in Fig.(9). The unit cell is composed of an inclusion material (phase I, iron) and a matrix material (phase II, epoxy), whose properties are provided in Table.1, which is identical to the example given in Section 5.1. Geometry features of the unit cell can be described by 4 parameters (see Fig.(9)) which involve: a, referring to the matrix edge length; b and c, giving the outer and inner diameter of the octagonal star inclusion, respectively; and finally, t, thickness of the unit cell. In this example, we fix 3 of the 4 geometry parameters : $a = 1$ mm, $b = 0.9$ mm and $t = 120$ μm, and we modify the inclusion geometry by affecting a range of values to c, inner diameter of the inclusion star, from $c = 0.1$ mm to $c = 0.9$ mm at an interval of 0.1 mm. This allows us to conduct parametric analysis on the unit cell which leads to the most favourable inclusion configuration with extended band gap.

Concerning the band gap analysis, we calculate band diagrams for antiplane elastic wave propagation by considering wave vectors on the boundary of the irreducible first Brillouin zone, which refers to the triangle zone $\Gamma - X - M - \Gamma$ as indicated in Fig.(6b) with the account for structure symmetry. Similar to the case in Section 5.1, we sweep the boundary $\Gamma - X - M - \Gamma$ through 58 equidistant, discrete points along the path. Then, on each section of the path which means $\Gamma - X$, $X - M$ and $M - \Gamma$, we implement Floquet-periodic boundary conditions whose expressions are identical to those given in Section 5.1.

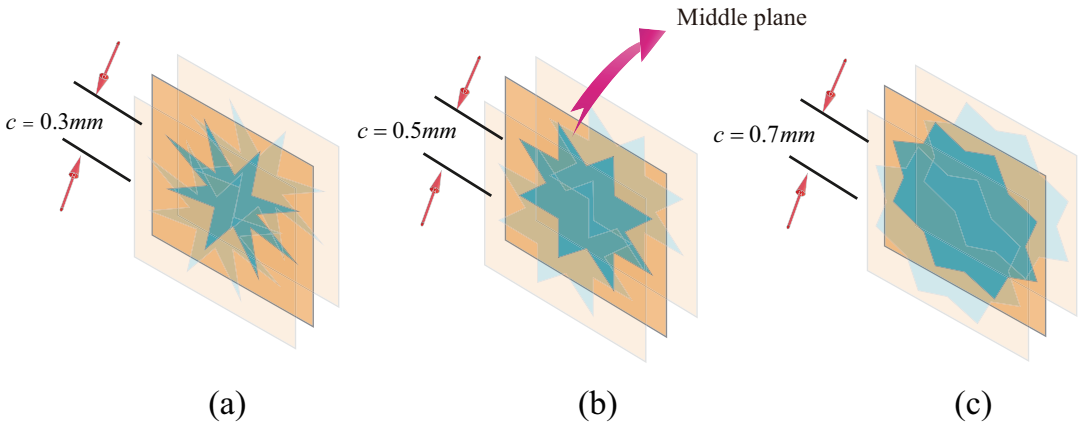

Figure 10: Unit cell configuration with (a) $c = 0.3$ mm (b) $c = 0.5$ mm (c) $c = 0.7$ mm

We report result band diagrams in Fig.(11(a)-(c)) for inclusion configurations with $c = 0.3$ mm, 0.5 mm and 0.7 mm, respectively. Position of the first full band gap is highlighted on each band diagram. We note therefore the first band gap in the frequency range $[596.25, 641.69]$ kHz, $[629.51, 741.69]$ kHz and $[694.76, 772.47]$ kHz for cases with $c = 0.3$ mm, 0.5 mm and 0.7 mm, respectively. Evolution of the first bang gap range as function of c is depicted in Fig.(12). With increasing values of c, the octagonal inclusion star gradually expands in size. Meanwhile, the resulting band gap range first increases, then decreases after reaching the maximum at $c = 0.5$ mm.

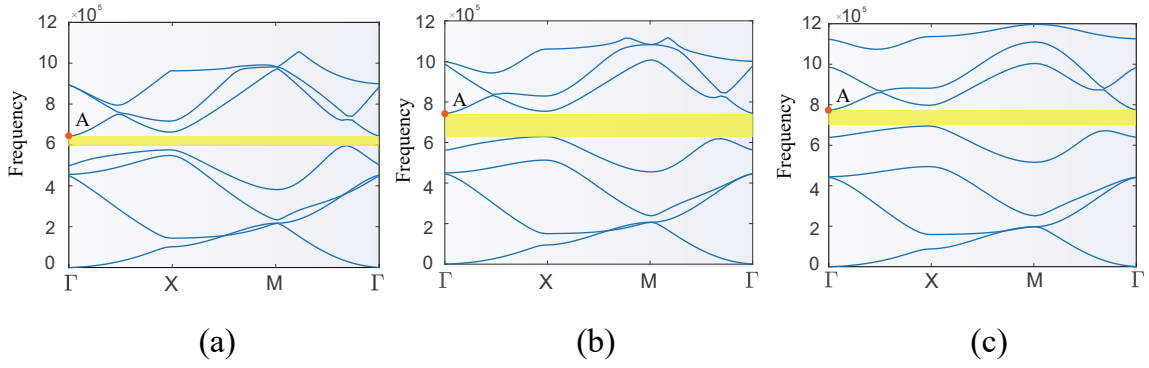

Figure 11: Band diagrams for (a) $c = 0.3$ mm, (b) $c = 0.5$ mm, (c) $c = 0.7$ mm.

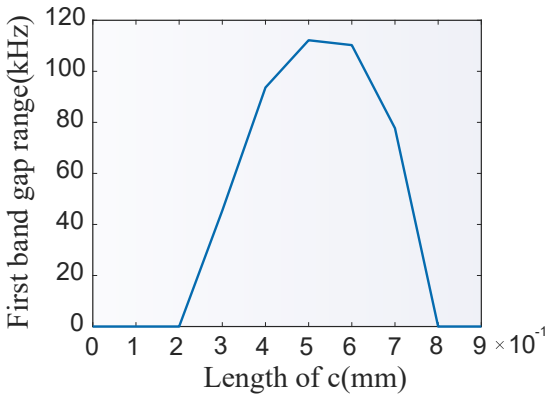

Figure 12: The trend of the first order gap with the increase of c

To understand the formation mechanism of the band gap and its evolution following the inclusion geometry, we conduct vibration modal analysis and investigate the mode shape configurations at point A (highlighted in Fig.(11)) of the associated unit cell structure for the 3 tested cases with $c = 0.3$ mm, 0.5 mm and 0.7 mm. The obtained mode shapes in terms of the vibration amplitude are depicted in Fig.(13). It can be observed that the $c = 0.5$ mm case presents the most significant out-of-plane vibration. By superimposing the mode shape Fig.(13(b)) on its corresponding unit cell configuration (Fig.(10)(b)), we deduce that the larger band gap (Fig.(11(b))) originates from the energy absorbing vibration of the matrix, induced by the local translational resonance in z direction under wave scattering effect due to the octagonal star inclusion.

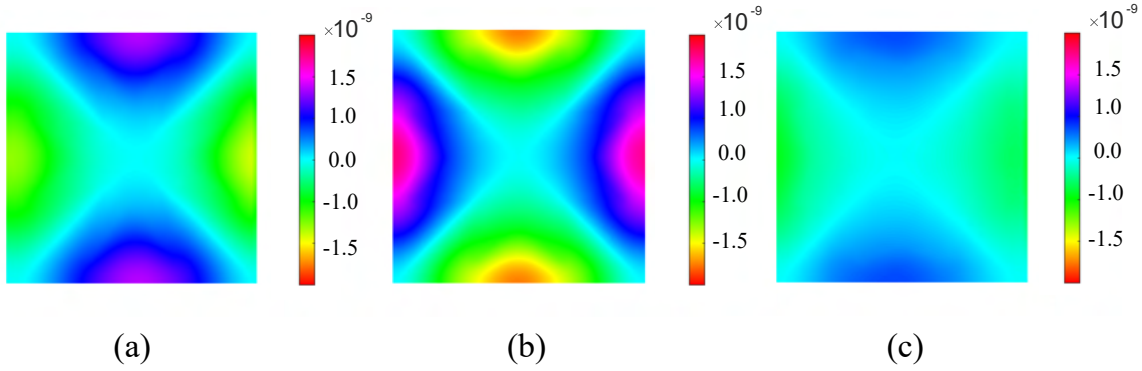

Figure 13: Mode shape based on displacement in z, which gives indication of the out-of-plane vibration amplitude, with (a) $c = 0.3$ mm, (b) $c = 0.5$ mm, (c) $c = 0.7$ mm.

5.3 Influence of microstructure effect and higher order theory on mesh quality

This example is aimed to further confirm the adaptability and robustness of the proposed T3 micro plate FEM framework for bandgap analysis. The test scenario is inspired by the recent work ([48]), which investigates wave attenuation effects of hybrid auxetic metamaterials. Here, we adopt the unit cell architecture prescribed ([48]) in which combines reentrant and anti-chiral geometries. Then, by varying the micro plate thickness, we demonstrate that the bandgap solution based on the couple stress formulation gradually converges towards solution from classical theory.

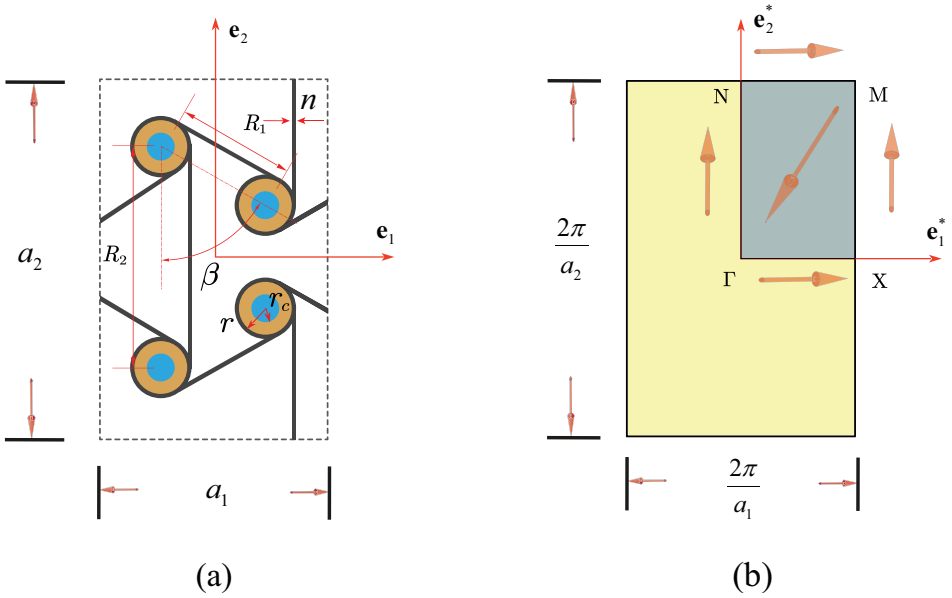

Figure 14: (a)Chiral Symmetric Unit Cell (b)Irreducible first Brillouin zone in the reciprocal lattice

The hybrid auxetic metastructure under consideration is depicted in Fig.(14a), it involves a basic auxetic reentrant lattice combined with anti-chiral components. The ring node of the anti-chiral structure is filled with an elastomer coated mass inclusion. The unit cell dimension is given by its side lengths along x and y axis, denoted by a_1 and a_2, respectively. Distance between the centres of two horizentally and verticallay neighbouring rings is given by R_1 and R_2, respectively. Chiral angle of the lattice is defined by β. Width of the outermost black ring is n. The inclusion is composed of a core material embedded in an elastomer matrix. Radius of the core and of the entire inclusion are denoted by r_c and r, respectively. Side lengths of the unit cell can also be written as:

$$\begin{aligned} a_1 &= 2R_1 \sin\beta \ , \\ a_1 &= 2\left(R_2 - R_1\cos\beta\right) \ . \end{aligned} \tag{58}$$

Concerning the material composition of the solid inclusion, material parameters of the core are given as follows: elastic modulus $E = 177.33$ Gpa; Poisson ratio $\mu = 0.27$; density $\rho = 7$ g/cm^3; material length scale parameter $l = 6.76$ μm. Then, material properties of the inclusion matrix are as follows: $E = 3.3$ Gpa, $\mu = 0.33$, $\rho = 1.18$ g/cm^3, $l = 16.93$ μm. Regarding material parameters of the lattice structure, we have: $E = 193$ Gpa, $\mu = 0.28$, $\rho = 7.8$ g/cm^3, $l = 6.8$ μm ([49]).

Wave propagation in periodic medium can be analysed through investigation on the basic unit cell, whose dimension is $\frac{2\pi}{a_1} \times \frac{2\pi}{a_2}$ in the local coordinates according the local x and y directions. To conduct band gap analysis, we calculate band diagrams based on wave vectors on the boundary of the irreducible Brillouin zone, which, by considering the anti-chiral symmetry of the unit cell structure, reduces to the quadrilateral area depicted in grey colour in Fig.(14b). Wave vectors are analysed on discrete points through the path $\Gamma - X - M - \Gamma - N - M$, also indicated in Fig.(14b).

We first discuss the difference in band gap solutions between the proposed modified couple stress framework and the classical theory. It is worth noting that methods based on classical theory do not incorporate tensors of couple stress and symmetric curvature, and therefore, cannot account for size effects which may emerge on microscopic problems. As a result, it is expected to observe divergence

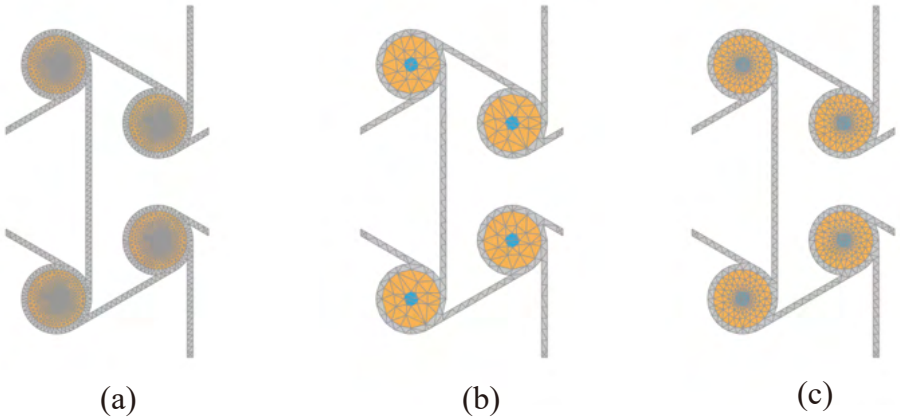

Figure 15: (a)Finest grid (b)Coarse grid (c)Medium fine mesh

between the two theories when it comes to structures of very small sizes, which have been included in the test scenario.

Here, the following unit cell size parameters are used: $r = 5$ mm, $r_c = 1.25$ mm, $n = 1$ mm, $R_1 = 20$ mm, $R_2 = 40$ mm, $\beta = 60°$. We conduct a series of band gap calculations by considering increasing unit cell thicknesses $t = 20\ \mu\text{m}, 60\ \mu\text{m}, 120\ \mu\text{m}$ and $200\mu\text{m}$, using both the couple stress and classical methods. This allows us to compare the results from the two approaches. In addition, to ensure Mindlin plate assumptions, we set a_2 for each case of t such that $a_2 : t = 12 : 1$. Discretized unit cell is plotted in Fig.(15a). The result band gap diagrams based on the described methodology are given in Fig.(17), from which, we extract and report in Table 2 the frequency range of the first band gap, which compares the two numerical methods for different unit cell sizes:

Table 2: First band gap frequency range

Thickness	Proposed couple stress model	Classical theory
$20\mu m$	[1572.1, 2286.9] kHz	[1104.0, 1725.6] kHz
$60\mu m$	[433.05, 676.14] kHz	[367.99, 575.20] kHz
$120\mu m$	[193.85, 303.18] kHz	[183.99, 287.60] kHz
$200\mu m$	[111.63, 175.02] kHz	[110.40, 172.56] kHz

Comparison of the two models shows that on smaller problems, microstructure effects become increasingly obvious. Both position and band width of the first band gap diverge with decreased problem sizes ($t \leqslant 120\ \mu$m in the present example). This divergence is depicted in Fig.(16) which compares the couple stress model and the classical theory model in terms of the band width of the first band gap on varying problem sizes. On the other hand, we note also that the microstructure effects tend to disappear with increased problem size. Here, with $t \geqslant 120\ \mu$m results from the two methods tend to coincide. This observation confirms improved adaptability of the proposed couple stress model for size effects, since it accounts for microstructure effects which become important in micro mechanics, while offering natural coherence with classical theory on larger problem sizes.

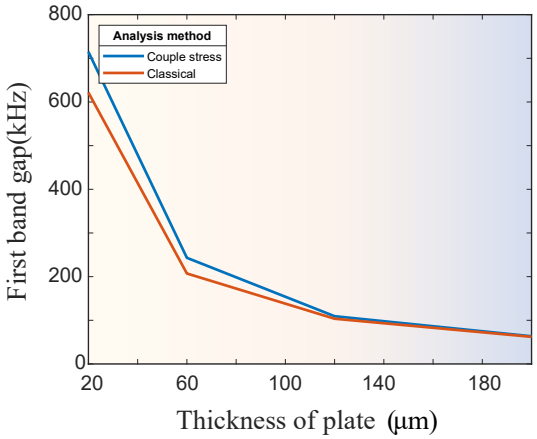

Figure 16: Couple stress model *versus* the classical theory model: band width of the first band gap diverges with decreased problem size ($t \leqslant 120$ μm), due to microstructure effects that emerge on problems of small sizes.

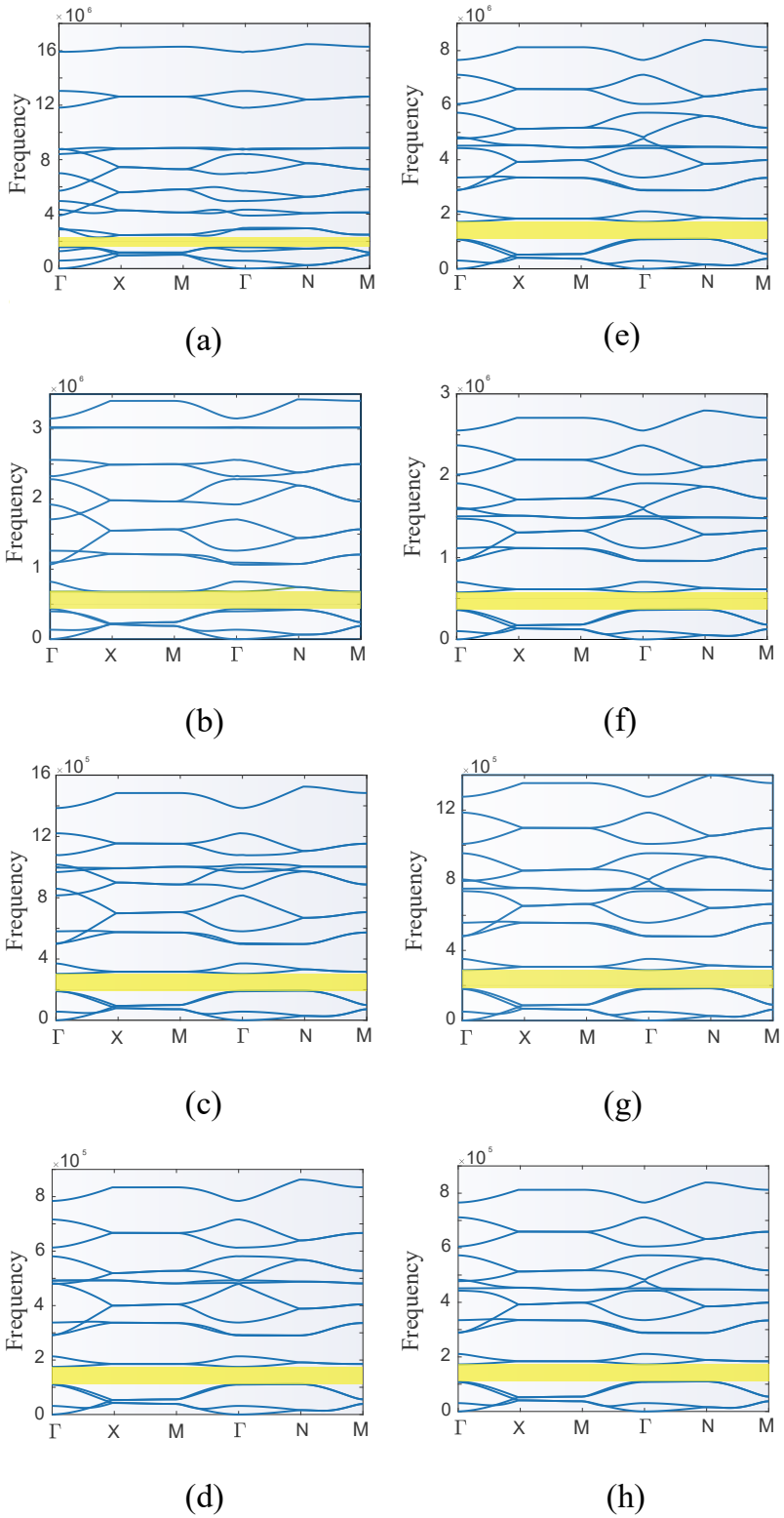

Figure 17: (a-d)Band gap diagram which calculate by modified couple stress theory when the thickness t is 20 μm, 60 μm, 120 μm, 200 μm (e-h)Band gap diagram which calculate by classical theory when the thickness t is 20 μm, 60 μm, 120 μm, 200 μm

To further compare the couple stress and classical theory models, we next investigate the impact of mesh refinement on the accuracy of respective methods. We set the plate thickness to $t = 120$ μm, and prescribe 3 levels of mesh refinement as shown in Fig.(15). We then perform band gap analysis using the couple stress and classical theory models to examine their dependence on mesh refinement. Resulting band gap diagrams are reported in Fig.(18)-(19), which refer to cases with refined and coarse meshes, respectively. Meanwhile on each mesh refinement, we further check if any difference is present between the couple stress and classical theory methods.

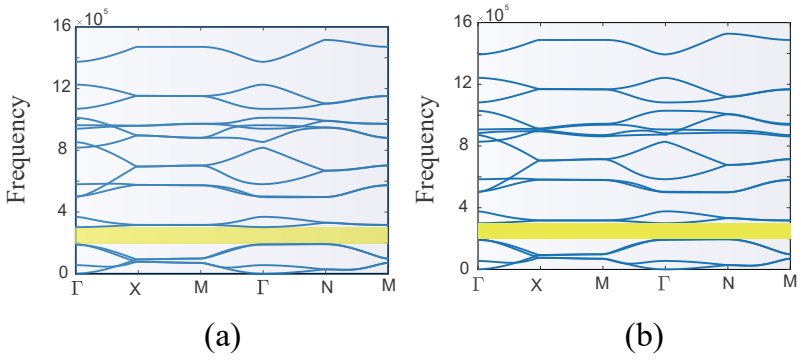

Figure 18: Band gap diagrams calculated using **refined** mesh: (a) by modified couple stress method, (b) by classical theory model. Concordant results are observed in diagrams (a) and (b).

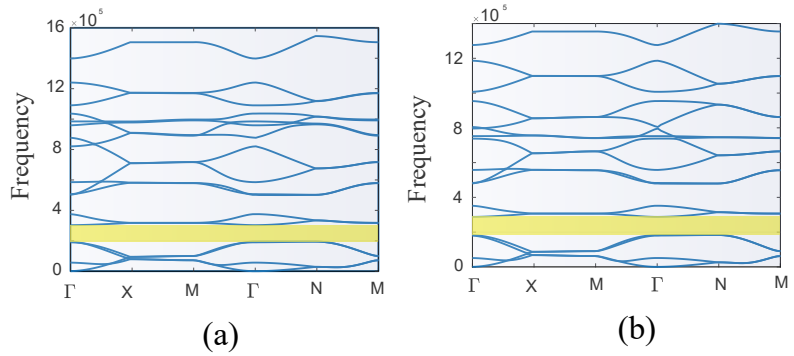

Figure 19: Band gap diagrams calculated using **coarse** mesh: (a) by modified couple stress method, (b) by classical theory model. Diagrams (a) and (b) are different.

We note that on the refined mesh (see diagrams in Fig.(18)), both methods produce consistent result, however in the case of coarse mesh (see diagrams in Fig.(19)), band diagram calculated with the classical theory (Fig.(19b)) presents slight difference *versus* the couple stress counterpart (Fig.(19a)). Furthermore, comparison between Fig.(18a) and Fig.(19a) does not reveal notable difference, which means the proposed couple stress model does not exhibit dependence on mesh refinement, while the classical model does. This advantage can be explained by the use of higher-order form functions associated with the C_1 continuous interpolation scheme, that we implemented in the couple stress micro plate finite element. In contrary, the classical theory model is based on low-order interpolation scheme, whose accuracy is highly sensible to the mesh quality.

In conclusion, the following advantages of the proposed framework have been confirmed with the present example. First, the proposed method is highly versatile to deal with microstructures of complex geometry. Secondly, it accounts for microstructure effects for problems of small sizes while remaining

compatible with classical theories of continuum mechanics. In the end, it offers improved robustness since its high-order interpolation scheme makes it highly independent on mesh quality.

6 Conclusion

We proposed in this work a numerical framework for the calculation of elastic wave band gaps for periodic composite micro plates based on T3 Mindlin micro plate finite elements. The proposed framework combines the couple stress elasticity theory which incorporates material length scale in the constitutive description, and non-conforming T3 Mindlin micro plate finite element that we implemented. The framework allows solving band problems of composite micro plates across length scales. This involves both problems at very small scale lengths with the presence of size effects, and those beyond the millimetre level for which size effects are negligible. Concerning the finite element used in the work, the triangular element topology offers improved flexibility to discretize complex microstructures, and the non-conforming element formulation provides nodal continuity of displacements, and their first and second derivatives which are required by the couple stress continuum theory. The present work is the first numerical contribution on the band gap calculation using couple-stress Mindlin plate finite element. The framework can be complemented by implementing additional finite element types, such as shells, so as to expand the field of application to 2D periodic metastructures involving curvature.

Acknowledgement

The authors gratefully acknowledge the support from National Natural Science Foundation of China (Grant No. 12002086).

References

[1] K. Billon, I. Zampetakis, F. Scarpa, M. Ouisse, E. Sadoulet-Reboul, M. Collet, A. Perriman, and A. Hetherington. Mechanics and band gaps in hierarchical auxetic rectangular perforated composite metamaterials. *Composite Structures*, 160:1042–1050, 2017.

[2] B. Cai and P. Wei. Surface/interface effects on dispersion relations of 2d phononic crystals with parallel nanoholes or nanofibers. *Acta Mechanica*, 224(11):2749–2758, 2013.

[3] Z. B. Cheng, Y. G. Xu, and L. L. Zhang. Analysis of flexural wave bandgaps in periodic plate structures using differential quadrature element method. *International Journal of Mechanical Sciences*, 100:112–125, 2015.

[4] S. A. El-Naggar, S. I. Mostafa, and N. H. Rafat. Complete band gaps of phononic crystal plates with square rods. *Ultrasonics*, 52(4):536–542, 2012.

[5] G. Zhang and X.-L. Gao. Band gaps for wave propagation in 2-d periodic three-phase composites with coated star-shaped inclusions and an orthotropic matrix. *Composites Part B: Engineering*, 182:107319, 2020.

[6] J. C. Hsu and T. T. Wu. Efficient formulation for band-structure calculations of two-dimensional phononic-crystal plates. *Physical Review B Condensed Matter*, 74(14):2952–2961, 2006.

[7] M. S. Kushwaha, P. Halevi, L. Dobrzynski, and B. Djafari-Rouhani. Acoustic band structure of periodic elastic composites. *Physical Review Letters*, 71(13):2022–2025, 1993.

[8] X. Liu, Z. Shi, and Y. L. Mo. Attenuation zones of initially stressed periodic mindlin plates on an elastic foundation. *International Journal of Mechanical Sciences*, 115-116:12–23, 2016.

[9] M. M. Sigalas and E. N. Economou. Elastic waves in plates with periodically placed inclusions. *Journal of Applied Physics*, 75(6):2845–2850, 1994.

[10] E. B. Chin, A. A. Mokhtari, A. Srivastava, and N. Sukumar. Spectral extended finite element method for band structure calculations in phononic crystals. *The Journal of the Acoustical Society of America*, 149(4):A129–A129, 2021.

[11] Y. Chen and L. Wang. Periodic co-continuous acoustic metamaterials with overlapping locally resonant and bragg band gaps. *Applied Physics Letters*, 105(19):5044, 2014.

[12] A. O. Krushynska, M. Miniaci, F. Bosia, and N. M. Pugno. Coupling local resonance with bragg band gaps in single-phase mechanical metamaterials. *Extreme Mechanics Letters*, 12:30–36, 2017.

[13] A. O. Krushynska, M. Miniaci, V. G. Kouznetsova, and M. G. Geers. Multilayered inclusions in locally resonant metamaterials: Two-dimensional versus three-dimensional modeling. *Journal of Vibration and Acoustics*, 139(2), 2017.

[14] M. Kadic, T. Frenzel, and M. Wegener. When size matters. *Nature Physics*, 14(1):8–9, 2018.

[15] G. Y. Zhang and X.-L. Gao. Elastic wave propagation in 3-d periodic composites: Band gaps incorporating microstructure effects. *Composite Structures*, 204(NOV.):920–932, 2018.

[16] A. Madeo, P. Neff, I.-D. Ghiba, L. Placidi, and G. Rosi. Band gaps in the relaxed linear micromorphic continuum. *ZAMM-Journal of Applied Mathematics and Mechanics/Zeitschrift für Angewandte Mathematik und Mechanik*, 95(9):880–887, 2015.

[17] A. L. Chen and Y. S. Wang. Size-effect on band structures of nanoscale phononic crystals. *Physica E: Low-dimensional Systems and Nanostructures*, 44(1):317–321, 2012.

[18] R. Rostami, M. Mohammadimehr, M. Ghannad, and A. Jalali. Forced vibration analysis of nanocomposite rotating pressurized microbeam reinforced by CNTs based on MCST with temperature-variable material properties. *Theoretical and Applied Mechanics Letters*, 8(2):97–108, 2018.

[19] S. K. Jena, R. Mundari, and S. Chakraverty. Vibration of microstructural elements. In *New Paradigms in Computational Modeling and Its Applications*, pages 35–44. Elsevier, 2021.

[20] D. Hou, L. Wang, J. Yan, and K. M. Liew. Vibration analysis of a strain gradient plate model via a mesh-free moving kriging interpolation method. *Engineering Analysis with Boundary Elements*, 135:156–166, February 2022.

[21] S. Markolefas and D. Fafalis. Strain gradient theory based dynamic mindlin-reissner and kirchhoff micro-plates with microstructural and micro-inertial effects. *Dynamics*, 1(1):49–94, July 2021.

[22] S. M. Mousavi and J. Paavola. Analysis of plate in second strain gradient elasticity. *Archive of Applied Mechanics*, 84(8):1135–1143, 2014.

[23] W. Chen and X. Li. A new modified couple stress theory for anisotropic elasticity and microscale laminated kirchhoff plate model. *Archive of Applied Mechanics*, 84(3):323–341, 2013.

[24] T. Q. Thai, X. Zhuang, and T. Rabczuk. A nonlinear geometric couple stress based strain gradient kirchhoff–love shell formulation for microscale thin-wall structures. *International Journal of Mechanical Sciences*, 196:106272, 2021.

[25] Y. Shang, H.-P. Wu, S. Cen, and C.-F. Li. An efficient 4-node facet shell element for the modified couple stress elasticity. *International Journal for Numerical Methods in Engineering*, 123(4):992–1012, November 2021.

[26] J. H. Argyris, I. Fried, and D. W. Scharpf. The TUBA family of plate elements for the matrix displacement method. *The Aeronautical Journal*, 72(692):701–709, 1968.

[27] K. Bell. A refined triangular plate bending finite element. *International Journal for Numerical Methods in Engineering*, 1(1):101–122, 1969.

[28] R. Clough and J. Tocher. Finite element stiffness matrices for analysis of plate bending. In *Matrix Methods in Structural Mechanics*, pages 515–545, 1965.

[29] M. J. D. Powell and M. A. Sabin. Piecewise quadratic approximations on triangles. *ACM Transactions on Mathematical Software*, 3(4):316–325, December 1977.

[30] J. Torabi, R. Ansari, and M. Darvizeh. A c1 continuous hexahedral element for nonlinear vibration analysis of nano-plates with circular cutout based on 3d strain gradient theory. *Composite Structures*, 205:69–85, 2018.

[31] S.-A. Papanicolopulos, A. Zervos, and I. Vardoulakis. A three-dimensional c1 finite element for gradient elasticity. *International Journal for Numerical Methods in Engineering*, 77(10):1396–1415, 2009.

[32] A. Zervos, S.-A. Papanicolopulos, and I. Vardoulakis. Two finite-element discretizations for gradient elasticity. *Journal of Engineering Mechanics*, 135(3):203–213, 2009.

[33] J. Zhao, W. J. Chen, and S. H. Lo. A refined nonconforming quadrilateral element for couple stress/strain gradient elasticity. *International Journal for Numerical Methods in Engineering*, 85(3):269–288, 2010.

[34] G. Bazeley, Y. K. Cheung, B. M. Irons, and O. C. Zienkiewicz. Triangular elements in plate bending - conforming and non-conforming solutions. In *Matrix Methods in Structural Mechanics*, pages 547–576, 1965.

[35] F. Yang, A. Chong, D. Lam, and P. Tong. Couple stress based strain gradient theory for elasticity. *International Journal of Solids and Structures*, 39(10):2731–2743, 2002.

[36] H. M. Ma, X.-L. Gao, and J. N. Reddy. A non-classical mindlin plate model based on a modified couple stress theory. *Acta Mechanica*, 220(1-4):217–235, 2011.

[37] G. Y. Zhang, Y. L. Qu, X.-L. Gao, and F. Jin. A transversely isotropic magneto-electro-elastic timoshenko beam model incorporating microstructure and foundation effects§. *Mechanics of Materials*, page 103412, 2020.

[38] G. Y. Zhang, X.-L. Gao, and S. R. Ding. Band gaps for wave propagation in 2-d periodic composite structures incorporating microstructure effects. *Acta Mechanica*, 229(10):4199–4214, 2018.

[39] C. Kittel. Introduction to solid state physics. 1976.

[40] R. D. Mindlin. Influence of rotatory inertia and shear on flexural motions of isotropic, elastic plates. 1951.

[41] R. J. Melosh. A stiffness matrix for the analysis of thin plates in bending. *Journal of the Aerospace Sciences*, 28(1):34–42, January 1961.

[42] R. J. Melosh. Basis for derivation of matrices for the direct stiffness method. *AIAA Journal*, 1.7:1631–1637, January 1963.

[43] J. N. Reddy. *An Introduction to the Finite Element Method*. McGraw-Hill Education, 2005.

[44] V. F. Dal Poggetto and A. L. Serpa. Elastic wave band gaps in a three-dimensional periodic metamaterial using the plane wave expansion method. *International Journal of Mechanical Sciences*, 184:105841, 2020.

[45] D. C. Lam, F. Yang, A. Chong, J. Wang, and P. Tong. Experiments and theory in strain gradient elasticity. *Journal of the Mechanics and Physics of Solids*, 51(8):1477–1508, 2003.

[46] S. K. Park and X.-L. Gao. Bernoulli–euler beam model based on a modified couple stress theory. *Journal of Micromechanics and Microengineering*, 16(11):2355, 2006.

[47] M. S. Kushwaha, P. Halevi, L. Dobrzynski, and B. Djafari-Rouhani. Acoustic band structure of periodic elastic composites. *Physical review letters*, 71(13):2022, 1993.

[48] D. Qi, H. Yu, W. Hu, C. He, W. Wu, and Y. Ma. Bandgap and wave attenuation mechanisms of innovative reentrant and anti-chiral hybrid auxetic metastructure. *Extreme Mechanics Letters*, 28:58–68, 2019.

[49] G. Y. Zhang and X.-L. Gao. Band gaps for flexural elastic wave propagation in periodic composite plate structures based on a non-classical mindlin plate model incorporating microstructure and surface energy effects. *Continuum Mechanics and Thermodynamics*, 2019.

A non-classical couple stress based Mindlin plate finite element framework for tuning band gaps of periodic composite micro plates

Supplementary information

To investigate the convergence properties of the implemented 3-node couple-stress Mindlin plate element, we carried out a series of tests that we report here in this section. We are particularly interested in assessing the presence of dependence on the mesh refinement and quality, in the context of couple-stress continuum theory.

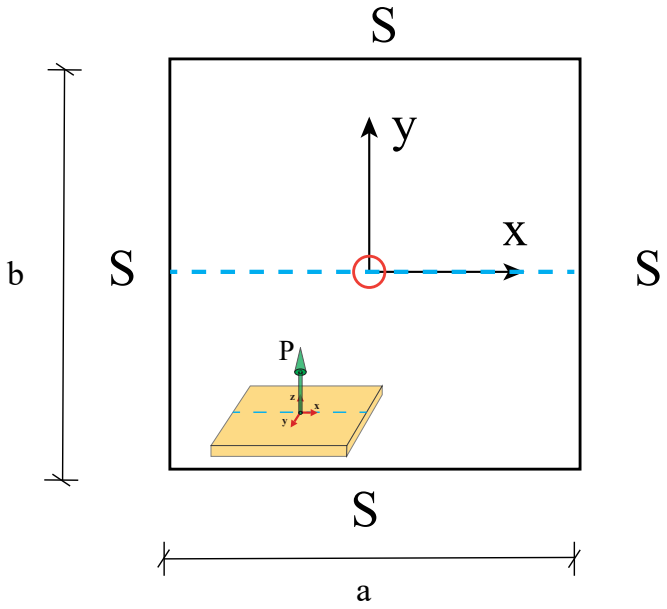

Figure 1: The test scenario: a rectangular plate of dimension $a \times b \times h$, with h the thickness, constrained on the 4 edges and subject to out-of-plane concentrated load at its centre. Deflections and rotations will be calculated on nodes along the cyan line $y = 0$ for the purpose of comparison

Test methodology

The test scenario is based on a plate structure constrained on the 4 edges and submitted to an out-of-plane concentrated load at the centre point as shown in Fig.(1). The load condition evokes both tensile and bending deformation to the plate. To investigate the dependence on the length scale parameter and its influence on the element's convergence behaviour, we assign a range of problem sizes that vary from micro to macro scale. This allows us to observe the appearance of size effects. Among the prescribed configurations, we select the one which presents the most significant size effect. We then assign to

this configuration a range of mesh refinements and qualities which allows assessing the presence of mesh dependence in the couple-stress plate model.

The test plate geometry is shown in Fig.(1). Its side lengths along x and y directions are denoted by a and b, then the plate thickness by h. The plate length versus thickness ratio is given by $a = b = 20h$. In this example, the boundary conditions are defined as follows: we let $w = 0$ and $\phi_x = 0$ at $x = -a/2$ and $x = a/2$ (left and right edges), respectively; then $w = 0$ and $\phi_y = 0$ at $y = -b/2$ and $y = b/2$ (lower and upper edges), respectively. A concentrated force $P = 0.1$N is applied at the centre of the plate. Material properties are given as: $E = 1.44$GPa, $\nu = 0.38$, $l = 17.6\mu m$, and $\rho = 1220kg/m^3$. We insist that the scale length parameter l is a material dependent parameter. The material considered the tests is resin, which gives $l = 17.6\mu m$.

Examination of size effect

To ensure that the value of $l = 17.6\mu m$ has significant effect in the couple-stress continuum model, we prescribe 2 groups of tests with different plate sizes. The first group with $h \geqslant l$, for instance, we have $h = l$, $h = 2l$, $h = 3l$, $h = 4l$, $h = 5l$, $h = 10l$. Then, the second group with $h < l$, we prescribe $h = 0.2l$, $h = 0.4l$, $h = 0.6l$, $h = 0.8l$. In total, 10 different plate sizes are considered separately and we conduct static analysis based on the boundary conditions described at the beginning of the methodology section.

Test group 1 with $h \geqslant l$

For the first test group composed of 6 cases with $h = l$, $h = 2l$, $h = 3l$, $h = 4l$, $h = 5l$, $h = 10l$, we extract the values of the out-of-plane deflection calculated along the line $y = 0$ (see Fig.(1) for the position of the line $y = 0$ and Fig.(2a) for the extracted deflection values). The result is compared with a Mindlin plate model based on classical continuum theory (see Fig.(2b)). In this test, both the couple-stress and classical theory models are discretized with a 40×40 mesh, as shown in Fig.(9e).

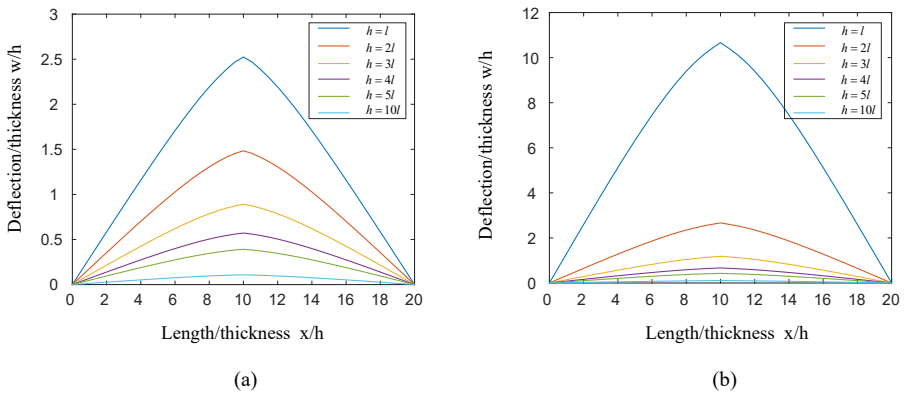

Figure 2: Out-of-plane deflections are extracted along the line $y = 0$, the result is reported in (a) for modified couple-stress plate model, and (b) for classical theory model

The shape of the obtained curves are obvious to interpret: both models let appear the highest deflection at the plate centre, which corresponds to the loading point. We notice that with larger problem sizes (as h increases towards $h = 10l$), the couple-stress model and classical theory model tend to agree with each other. This is normal, and means that as the problem size approaches $h = 10l$, the scale length parameter $l = 17.6\mu m$ tends to become irrelevant in the couple-stress model, which progressively converges to the classical model. Similarly, we observe in Fig.(3) the same trend with the rotation angle ϕ_x that we calculate along the line $y = 0$, for which as h increases towards $h = 10l$, the couple-stress model tends to converge towards the classical model. For small size problems, on the contrary, size effects become increasingly obvious with h approaching $h = l$. Among the tested configurations, the case with $h = l$ reveals the most significant difference between the couple-stress and classical models.

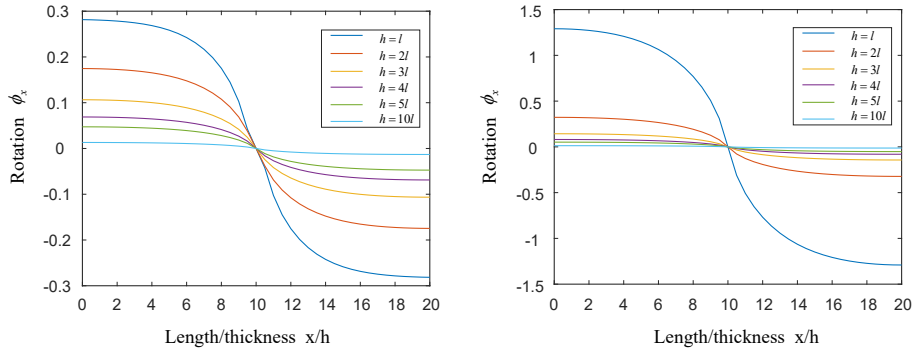

Figure 3: Rotations are calculated along the line $y = 0$, the result is reported in (a) for modified couple-stress plate model, and (b) for classical theory model

Test group 2 with $h < l$

The second test group investigates the situation with $h < l$. Although one may question about the physical relevance of such situations, they offer an insight into the limit of the couple-stress model dealing with plate dimensions smaller than the scale length from the numerical point of view. We therefore considered 4 cases with $h = 0.2l$, $h = 0.4l$, $h = 0.6l$, $h = 0.8l$, respectively. The test scenario remains identical to the first test group.

We report in Fig.(4) the out-of-plane deflections calculated along the line $y = 0$ from the deformed plate. The result is presented in Fig.(4a) for the couple-stress Mindlin micro plate model, then in Fig.(4b) for classical elasticity theory Mindlin plate model and in Fig.(4c) for couple-stress analytical model based on Fourier series expansion. Significant size effects can be confirmed by comparing Fig.(4a) and Fig.(4b). Then, good agreement is observed between the couple-stress numerical and analytical models by comparing Fig.(4a) and Fig.(4c). However, as the problem size approaches $h = 0.2l$,

the form of the curve can no longer represent the deformed shape of the micro plate, as expected by the load scenario.

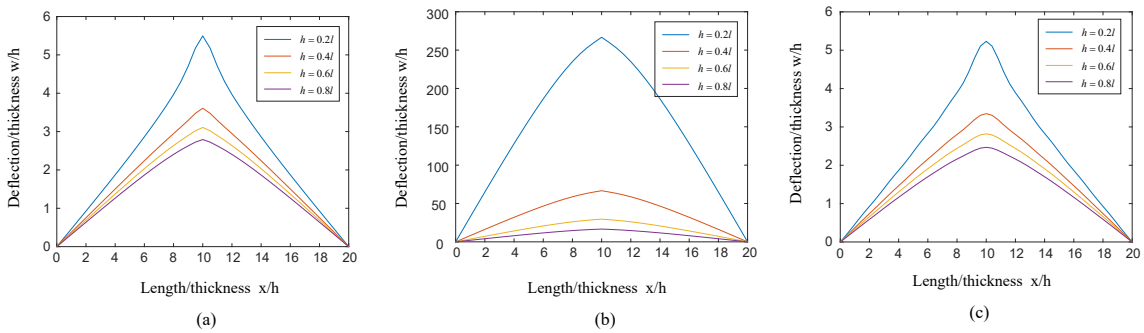

Figure 4: Out-of-plane deflections extracted along the line $y = 0$ from the deformed plate for 4 plate dimensions: $h = 0.2l$, $0.4l$, $0.6l$, and $0.8l$. The result is reported in (a) for the couple-stress Mindlin micro plate FEM model (b) classical elasticity Mindlin plate FEM model and (c) couple-stress analytical model based on Fourier series expansion.

Similar observations can be made on the rotation angles ϕ_x calculated along the line $y = 0$ from the deformed plate. We confirm strong size effect by the disagreement between the couple-stress and classical elasticity models (see Fig.(5a) and Fig.(5b)), and we observe good agreement between the couple-stress numerical and analytical models (see Fig.(5a) and Fig.(5c)). As the problem size decreases, brutal singularities appear on the curve, particularly for the case $h = 0.2l$ (see Fig.(5a)). This observation is confirmed by the analytical model (see Fig.(5c)), which suggests that the phenomenon results from the couple-stress theory rather than from numerical issues.

Therefore, we can predict significant couple-stress effects on problems whose dimension h is below the scale length parameter l. When h is significantly smaller than l, results from the couple-stress theory become unreliable. In other words, we suggest prescribing scale length parameters l with values below the problem's geometrical dimension. For plate structures, this means using l no greater than the plate thickness h.

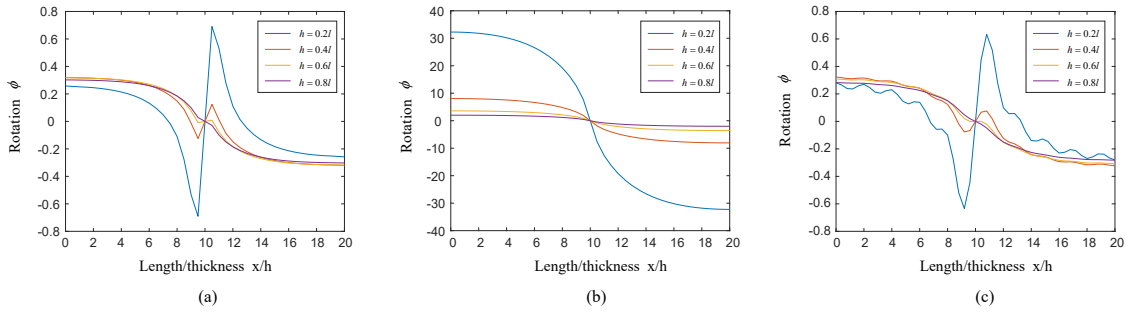

Figure 5: Rotations extracted along the line $y = 0$ from the deformed plate for 4 plate dimensions: $h = 0.2l$, $0.4l$, $0.6l$, and $0.8l$. The result is reported in (a) for the couple-stress Mindlin micro plate FEM model (b) classical elasticity Mindlin plate FEM model and (c) couple-stress analytical model based on Fourier series expansion.

Given the above conclusion, we adopt the configuration with $h = l$ in the following for the element convergence analysis. Using the tested scale length parameter $l = 17.6\mu m$,

the configuration $h = l$ presents the most significant size effect, with l no greater than h.

Convergence analysis

Based on the $h = l$ plate structure, the following tests are aimed to investigate the element convergence properties with respect to the mesh refinement and quality. We prescribe 6 mesh configurations, involving 5 structured meshes of different mesh densities and 1 unstructured mesh (free mesh).

Static analysis

We first focus on static analysis based on the load scenario described in the methodology section. 5 levels of mesh densities are prescribed using structured mesh topology: 4×4, 8×8, 12×12, 20×20 and 40×40 (see Fig.(9a-e)). For each density level, we calculate using both the 3-node triangular couple-stress plate element presented in the paper, and the 4-node rectangular plate element given in Appendix A. We also prescribe an unstructured mesh as shown in Fig.(9f) to assess if dependence on mesh quality is present.

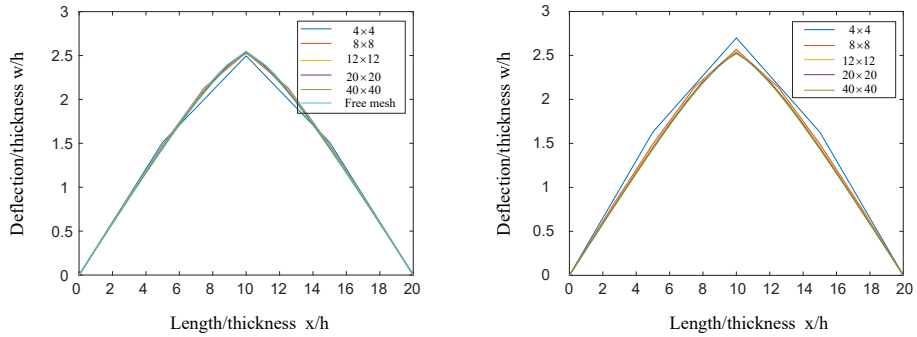

Figure 6: Out-of-plane deflections are calculated along the line $y = 0$, the result is reported in (a) for the 3-node triangular couple-stress element, and (b) for the 4-node rectangular couple-stress element

Fig.(6) presents the out-of-plane deflection along the line $y = 0$ for the different mesh configurations. We check if the results converge despite the different levels of mesh refinement, and we compare both the triangular element model (Fig.(6a)) and the rectangular element model (Fig.(6b)). We can see in both models, that the result does not depend on the mesh refinement, and the two models present satisfactory agreement. In this example, the 3-node triangular model shows comparable convergence with respect to the rectangular model.

Similarly, we present in Fig.(7) the values of nodal rotation ϕ_x calculated along the line $y = 0$. Comparison is carried out both with respect to the mesh refinement and the element type. Again, the 3-node triangular model shows good convergence despite the mesh configurations, and both element models present satisfactory agreement.

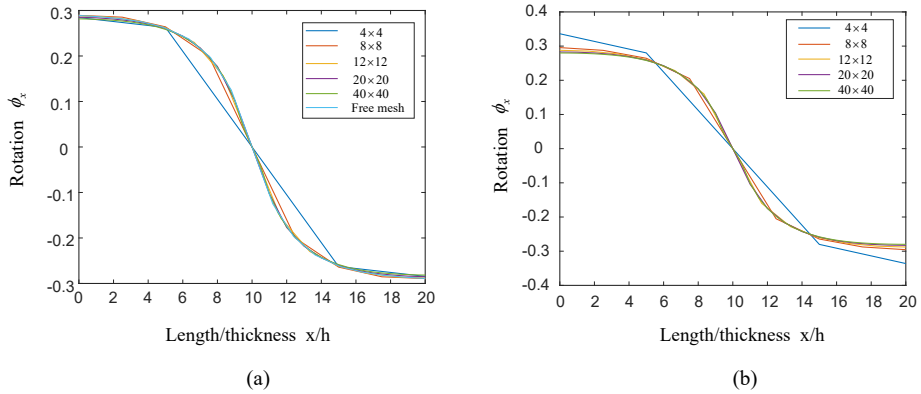

Figure 7: Rotations are calculated along the line $y = 0$, the result is reported in (a) for the 3-node triangular couple-stress element, and (b) for the 4-node rectangular couple-stress element

Natural frequency analysis

We also investigated the mesh dependence properties of the 3-node triangular couple-stress Mindlin plate element using natural frequency analysis. The problem is based on the same micro plate presented in the methodology section, with the aspect ratio characterized by $a = b = 20h$, with $h = l$. We remind that on this configuration, size effects inherent to the couple-stress continuum formulation are significant. In this example, 9 levels of mesh density is tested, they are given by 4×4, 8×8, 12×12, 20×20, 30×30, 40×40, 50×50, 60×60, and 70×70.

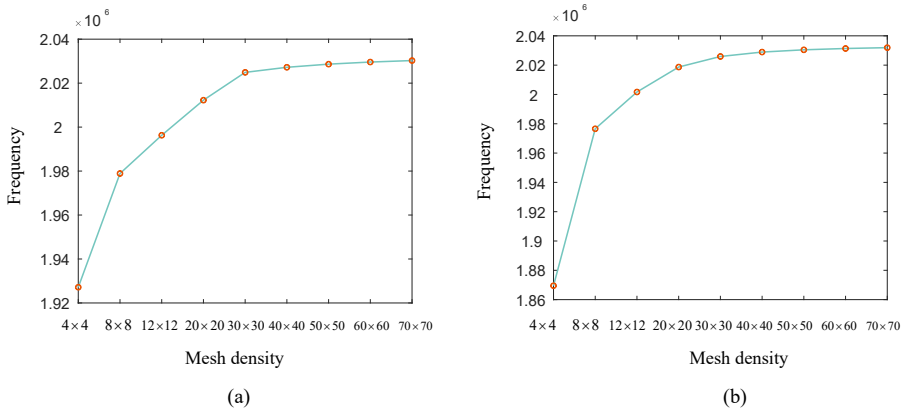

Figure 8: Natural frequencies with respect to different levels of mesh refinement. The result is reported in (a) for the 3-node triangular couple-stress element, and (b) for the 4-node rectangular couple-stress element

Fig.(8) presents the evolution of the calculated natural frequencies with respect to the considered levels of mesh density, both for the triangular element model (Fig.(8a)), and the rectangular element model (Fig.(8b)). Considering the two figures, we observe comparable convergence rate for the both models. Especially, with the highest tested mesh density (70×70), both results tend to the same value (2.032×10^6).

Numerical integration procedure

In all the convergence tests and numerical examples provided in the main article, we applied numerical integration based on a 3-point Gauss exact integration procedure. Reduced integration is not considered in this work. Details of the integration points are described in Fig.(10).

Summary

In this section, convergence properties of the implemented 3-node couple-stress Mindlin Plate element is examined based on a test scenario involving significant size effect. The convergence rate investigation requires discretizing the problem using several distinctive levels of mesh refinement, and the result is compared not only with respect to the tested mesh refinements, but also to a comparison model based on a different 4-node rectangular plate formulation. In the tested cases, the implemented 3-node couple-stress Mindlin Plate element showed satisfactory convergence properties, although the non-conforming formulation may lead to convergence difficulties, theoretically. The obtained result also presented good agreement with the 4-node rectangular plate modal.

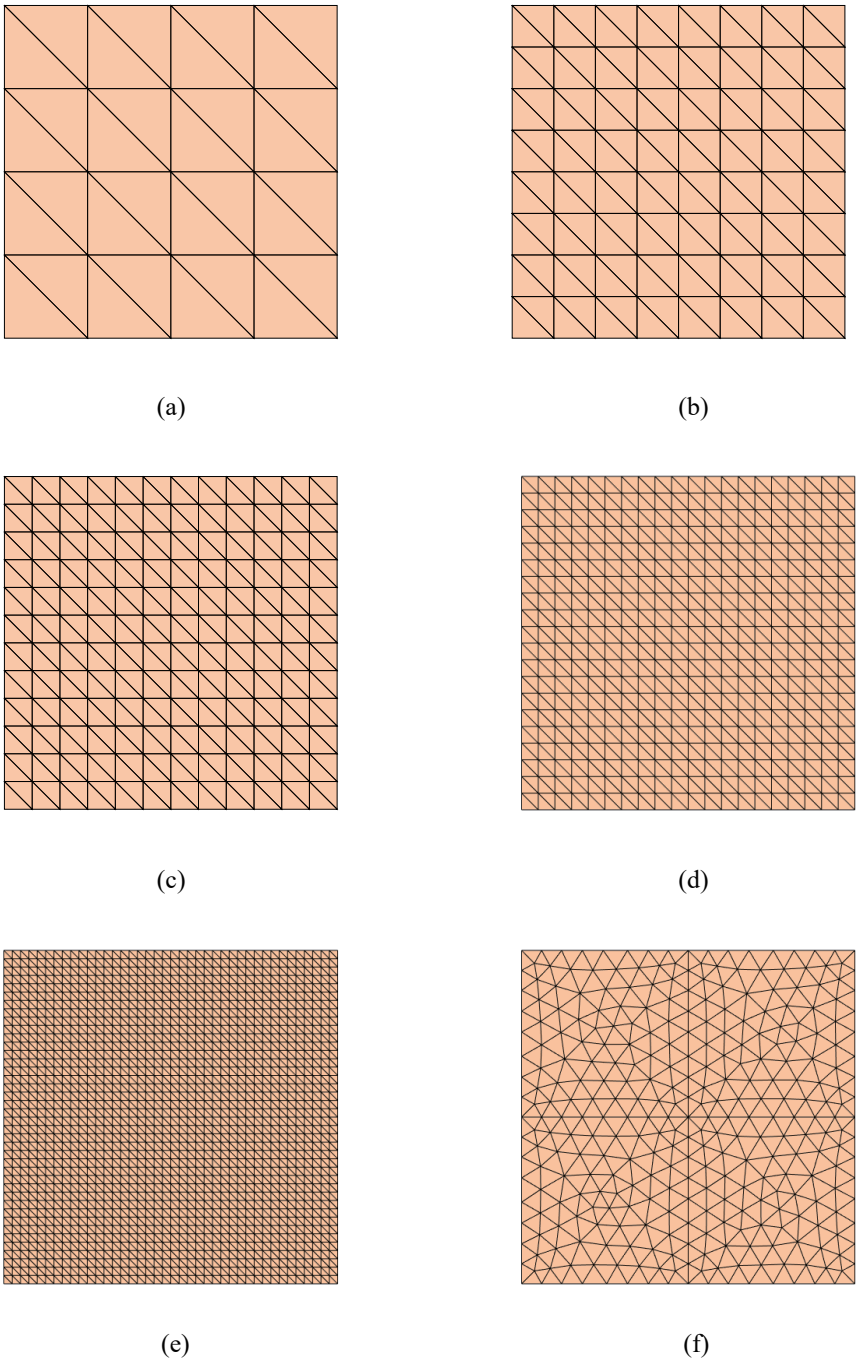

Figure 9: Mesh level include (a) 4×4 (b) 8×8 (c) 12×12 (d) 20×20 (e) 40×40 (f) free mesh

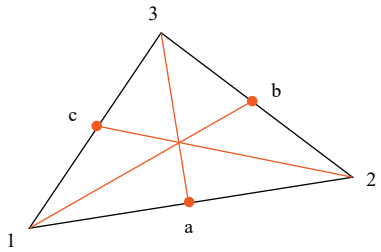

Points	L1	L2	L3	Weights
a	1/2	1/2	0	1/6
b	0	1/2	1/2	1/6
c	1/2	0	1/2	1/6

Figure 10: Gauss exact integration and the integration points used in the T3 Mindlin micro plate finite element.